Fizika Nizkikh Temperatur, 2010, v. 36, No. 6, p. 613–639

Optical spectroscopy of charge transfer transitions in multiferroic manganites, ferrites, and related insulators

(Review Article)

A.S. Moskvin

Ural State University, Ekaterinburg 620083, Russia
E-mail: alexandr.moskvin@usu.ru

R.V. Pisarev

A.F. Ioffe Physical Technical Institute, Russian Academy of Sciences, St. Petersburg 194021, Russia

Received February 21, 2010

We review results of theoretical and experimental studies of charge transfer (CT) transitions in multiferroic manganites, ferrites, and related insulators. Starting with a simple cluster model approach we address both one-center *p–d* and two-center *d–d* CT transitions, their polarization properties, the role played by structural parameters, orbital mixing, and spin degree of freedom. We analyze optical ellipsometry data in the spectral range of 0.6–5.8 eV in perovskite and hexagonal rare-earth manganites $RMnO_3$ and in orthorhombic manganites RMn_2O_5. We discuss two groups of iron oxides where Fe^{3+} ions occupy either only octahedral positions ($BiFeO_3$, orhoferrites $RFeO_3$ *et al*.) and materials with Fe^{3+} ions both in octahedral and tetrahedral positions (hematite α-Fe_2O_3, garnets RFe_5O_{12}, lithium ferrite $LiFe_5O_8$, $Ca_2Fe_2O_5$ *et al*.).

PACS: 78.20.Bh Theory, models, and numerical simulation;
78.20.Ci Optical constants;
75.50.Ee Antiferromagnetics;
77.80.–e Ferroelectricity and antiferroelectricity.

Keywords: multiferroic manganites, ferrites, related insulators, charge transfer transitions.

Contents

1. Introduction

Multiferroic materials with two or more coexisting order parameters are known since the 1960s, see review papers [1–4]. The possible interactions between different order parameters make these materials promising candidates for the development of new spintronics and optoelectronics devices. Good examples are the most actively studied rare-earth (R) hexagonal and perovskite manganites $RMnO_3$, and orthorhombic manganites RMn_2O_5 [5–9]. However, the majority of multiferroic materials extensively studied so far, possess magnetic transition temperatures far below room temperature. Though demonstrating interesting new physics, they most probably are of no interest for practical applications. Among the materials exhibiting multiferroic properties above room temperature, the complex iron oxides based on octahedrally and/or tetrahedrally coordinated Fe^{3+} ion are of interest, as their electronic structure with half-filled t_{2g}^3 and e_g^2 orbitals favors strong exchange interaction and the highest magnetic transition temperatures in comparison to other 3*d* transition-metal oxides. Examples of such materials are lithium ferrite $LiFe_5O_8$ in which the magnetoelectric effect [10] and the optical magnetoelectric effect [11] were observed, thin films of bismuth-substituted iron garnets $R_{1-x}Bi_xFe_5O_{12}$ with giant optical magnetoelectric effects [12], gallium ferrite $GaFeO_3$ [13–15], and the recently reported magnetoelectric hexaferrites $Ba_{0.5}Sr_{1.5}Zn_2Fe_{12}O_{22}$ [16] and $Ba_2Mg_2Fe_{12}O_{22}$ [17]. However, the most prominent multiferroic among all known iron oxides is the bismuth ferrite $BiFeO_3$ [18–20]. This material reveals unique multiferroic and optical properties that imply its potential as a photovoltaic material [21] and suggest it to be suitable for novel optoelectronic devices.

The experimental observations along with recent theoretical predictions of important electronic contributions to the multiferroic properties are a strong motivation for more detailed studies of the electronic structure of multiferroics, in particular, the nature of the low-energy optical electron–hole excitations. All these excitations are especially interesting because these could play a central role in multiband Hubbard models used for describing both the insulating state and the unconventional states developed under electron or hole doping. In general, optical experiments are a powerful bulk sensitive spectroscopy, allowing one to address the complete excitation spectrum. Because of the matrix element effect the optical response does provide only an indirect information about the density of states. Nevertheless it remains one of the most efficient technique for inspecting the electronic structure and energy spectrum.

However, no comprehensive analysis of the spectral features and mechanisms governing the optical response of different multiferroics have been reported yet. At the same time this kind of information is of primary importance for the elucidation of the actual electronic states and a theoretical understanding of the mechanism(s) of the strong magnetoelectric coupling, in particular, the role of the electronic contribution to the multiferroic properties which may be quite important and in some cases comparable to the lattice contribution [22,23]. Indeed, the mechanisms of electric polarization, including its spin-dependent part, and the mechanisms specifying the optical response in 3*d* oxides have much in common [23–25]. Both are dominated by the *p–d* and *d–d* charge-transfer effects that makes its theoretical and experimental study a challenging task.

It is now believed that the most intensive low-energy electron–hole excitations in insulating 3*d* oxides correspond to the charge transfer (CT) transitions while different phonon-assisted crystal field transitions are generally much weaker. Namely the CT transitions are considered as a likely source of the optical and magneto-optical response of the 3*d* metal-based oxide compounds in a wide spectral range of 1–10 eV, in particular, of the fundamental absorption edge. The low-energy dipole-forbidden *d–d* orbital excitations, or crystal field transitions, are characterized by the oscillator strengths which are smaller by a factor 10^2–10^3 than those for the dipole-allowed *p–d* CT transitions and usually correspond to contributions to the dielectric function ε_2 of the order of 0.001–0.01.

Despite CT transitions are well established concept in the solid state physics, their theoretical treatment remains rather naive and did hardly progress during last decades. Usually it is based on the one-electron approach with some 2*p*–3*d* or, at best, $2p \to 3d\,t_{2g}$, $2p \to 3d\,e_g$ CT transitions in 3*d* oxides. In terms of the Hubbard model, this is a CT transition from the nonbonding oxygen band to the upper Hubbard band. But such a simplified approach to CT states and transitions in many cases appears to be absolutely insufficient and misleading even for qualitative explanation of the observed optical and magneto-optical properties. First, one should generalize the concept of CT transitions taking into account the conventional transition between the lower and upper Hubbard bands which corresponds to an inter-site *d–d* CT transition, or intersite transition across the Mott gap.

Several important problems are hardly addressed in the current analysis of optical spectra, including the relative role of different initial and final orbital states and respective CT channels, strong intra-atomic correlations, effects of strong electron and lattice relaxation for CT states, the transition matrix elements, or transition probabilities, probable change in crystal fields and correlation parameters accompanying the charge transfer.

One of the central issues in the analysis of electron–hole excitations is whether low-lying states are comprised of free charge carriers or excitons. A conventional approach implies that if the Coulomb interaction is effectively screened and weak, then the electrons and holes are only weakly bound and move essentially independently as free charge-carriers. However, if the Coulomb interaction be-

tween electrons and holes is strong, excitons are believed to form, i.e., bound particle–hole pairs with strong correlation of their mutual motion.

This review was stimulated by the lack of detailed and reliable studies of electron–hole excitations and of a proper understanding of the relative role of *p–d* and *d–d* CT transitions in strongly correlated 3*d* oxides as parent systems for the high-temperature superconductive, colossal magnetoresistive [26] and multiferroic [6] materials. Hereafter, in this paper we report the results of theoretical and experimental investigations of *p–d* and *d–d* CT transitions and optical response in multiferroic manganites and ferrites aimed to study the near band gap electronic structure of these materials which is of primary importance for constructing appropriate Hubbard models and obtaining adequate theoretical description of their multiferroic properties. Given the complex phase diagram of this class of materials, studies of the CT states and transitions could uncover electronic states as potential contributors to giant multiferroicity and give an insight into physics governing the multiferroic properties.

Our efforts were focused on the theoretical and experimental studies of the low-energy CT bands in the spectral range 2–5 eV with a particular interest in the assignment variety of different CT states and CT transitions in the perovskite manganites and ferrites based on the distorted MeO_6 octahedra being a basic element of their crystalline and electronic structure. Then we present and discuss experimental results of optical ellipsometry for a number of multiferroic manganites and ferrites.

Some previously reported optical data on manganites and ferrites were in most cases obtained with the use of conventional reflection and absorption methods. We performed our study using a variable-angle spectroscopic ellipsometer as described elsewhere [27–31]. The technique of optical ellipsometry provides significant advantages over conventional reflection and transmittance methods in that it is self-normalizing and does not require reference measurements. The optical complex pseudodielectric function $\varepsilon = \varepsilon' - i\varepsilon''$ is obtained directly without the Kramers–Krönig transformation. From the measured ellipsometric angles ψ and Δ the pseudodielectric function is calculated as

$$\varepsilon^{ps} = \sin^2\theta\left[1+\tan^2\theta\left(\frac{1-\rho}{1+\rho}\right)^2\right], \qquad (1)$$

where $\rho = \tan\psi e^{i\Delta}$ and θ is the angle of incidence [27]. For isotropic crystals this function gives the value of the dielectric function of the material $\varepsilon = \varepsilon^{ps}$ if a surface roughness is taken into account properly. In the case of uniaxial crystals [28,29] the pseudodielectric function extracted from the measurements performed for two different orientations of the sample are a good approximation for the true dielectric function of the crystal. Thus, ε^{ps} measured with *p*-polarized light for a crystal with the optical axis *z* lying in the plane of incidence gives the value of ε_{zz} and, subsequently, of the extraordinary refractive and absorption indices. The value for $\varepsilon_{xx} = \varepsilon_{yy}$ and the ordinary refractive and absorption indices can be obtained in the same way when the optical axis is perpendicular to the plane of incidence.

In the case of biaxial crystal the pseudodielectric function (1) can be again a reasonable approximation, if the sample is properly oriented with one of the principle directions being perpendicular to the sample surface. In this case ε^{ps} is comprised by the projections of the components of dielectric tensor along the two principle directions lying in the plane of incidence [28]. Thus, for the large angles of incidence used in our experiments (θ = = 60°–72°) the spectral behavior of ε^{ps} represents mainly the spectral behavior of the dielectric function for light polarized along the direction parallel to the intersection of the sample surface and the plane of incidence. Thus, performing the ellipsometry measurements from different surfaces of the crystal, information of the spectral features of the dielectric function along all three principle directions of the crystal can be obtained. We note, that a more comprehensive treatment of the ellipsometry data [28] results in small corrections of the absolute values of the dielectric functions, without significant effect on the main spectral features.

This approximation, strictly speaking, is valid for large values of $|\varepsilon|$, i.e., in the range of strong absorption. In the low absorption range, however, the optical anisotropy is usually not resolved in ellipsometry measurements. Therefore, the pseudodielectric function can be used as an approximation for a dielectric function in the low absorption range.

Surface roughness and depolarization effects affect mostly the results in the low absorption range, but not the positions and the strength of intensive absorption bands. We note, that for all samples considered here the measurements were performed for several large angles of incidence θ. The coincidence of the dielectric functions extracted from these measurements points to the validity of the approach used.

The dielectric function ε was obtained in the range from 0.6 to 5.8 eV. The comparative analysis of the spectral behavior of ε_1 and ε_2 is believed to provide a more reliable assignment of the spectral features as compared to reflectivity measurements. The spectra were analyzed using the set of Lorentzian functions

$$\varepsilon = \varepsilon' - i\varepsilon'' = \varepsilon_0 + \sum \frac{f_j}{E_{0j}^2 - E^2 - iE\Gamma_j}, \qquad (2)$$

where f_j characterizes the strength of the *j*th oscillator with a central frequency E_{0j} and a half-width Γ_j, ε_0 is the dielectric susceptibility at $E = 0$.

The rest of the paper is organized as follows. In Sec. 2 we shortly address the electronic structure, the energy

spectrum of a MeO_6 cluster, and the one-center p–d CT transitions. Two-center d–d CT transitions are considered in Sec. 3. The experimental results of ellipsometric optical measurements for manganites and ferrites with a discussion are presented in Sec. 4 and 5, respectively.

2. One-center p–d charge transfer transitions in octahedral MeO_6 clusters

2.1. Electronic structure of octahedral 3d-metal-oxygen MeO_6 centers in perovskites

The electronic states in strongly correlated 3d oxides manifest both significant correlations and dispersional features. The dilemma posed by such a combination is the overwhelming number of configurations which must be considered in treating strong correlations in a truly bulk system. One strategy to deal with this dilemma is to restrict oneself to small clusters, creating model Hamiltonians whose spectra may reasonably well represent the energy and dispersion of the important excitations of the full problem. Naturally, such an approach has a number of principal shortcomings, including the boundary conditions, the breaking of local symmetry of boundary atoms, and so on. Nevertheless, this method provides a clear physical picture of the complex electronic structure and the energy spectrum, as well as the possibility of quantitative modelling. In a certain sense the cluster calculations might provide a better description of the overall electronic structure of insulating 3d oxides than the band structure calculations, mainly due to a better account for correlation effects.

Five Me3d and eighteen oxygen O2p atomic orbitals in octahedral MeO_6 complex with the point symmetry group O_h form both hybrid Me3d–O2p bonding and antibonding e_g and t_{2g} molecular orbitals (MO), and purely oxygen nonbonding $a_{1g}(\sigma)$, $t_{1g}(\pi)$, $t_{1u}(\sigma)$, $t_{1u}(\pi)$, $t_{2u}(\pi)$ orbitals (see, e.g., Refs. 32–34). Nonbonding $t_{1u}(\sigma)$ and $t_{1u}(\pi)$ orbitals with the same symmetry are hybridized due to the oxygen–oxygen O2$p\pi$–O2$p\pi$ transfer. The relative energy position of different nonbonding oxygen orbitals is of primary importance for the spectroscopy of the oxygen–3d-metal charge transfer. This is firstly determined by the bare energy separation $\Delta\varepsilon_{2p\pi\sigma} = \varepsilon_{2p\pi} - \varepsilon_{2p\sigma}$ between O2$p\pi$ and O2$p\sigma$ electrons.

Since the O2$p\sigma$ orbital points towards the two neighboring positive 3d ions, an electron in this orbital has its energy lowered by the Madelung potential as compared with the O2$p\pi$ orbitals, which are oriented perpendicular to the respective 3d–O–3d axes. Thus, Coulomb arguments favor the positive sign of the π–σ separation $\varepsilon_{p\pi}$–$\varepsilon_{p\sigma}$ which numerical value can be easily estimated in frames of the well-known point charge model, and appears to be of the order of 1.0 eV. In a first approximation, all the $\gamma(\pi)$ states $t_{1g}(\pi)$, $t_{1u}(\pi)$, $t_{2u}(\pi)$ have the same energy. However, the O2$p\pi$–O2$p\pi$ transfer yields the energy correction to bare energies with the largest value and positive sign for the $t_{1g}(\pi)$ state. The energy of the $t_{1u}(\pi)$ state drops due to a hybridization with the cation 4p $t_{1u}(\pi)$ state. In other words, the $t_{1g}(\pi)$ state is believed to be the highest in energy nonbonding oxygen state. For illustration, in Fig. 1 we show the energy spectrum of the 3d–2p manifold in the octahedral complexes MeO_6 with the relative energy position of the levels according to the quantum chemical calculations [35] for the FeO_6^{9-} octahedral complex in a lattice environment typical for perovskites such as $LaFeO_3$ and $LaMnO_3$. It should be emphasized once more that the top of the oxygen electron band is composed of O2$p\pi$ nonbonding orbitals that predetermines the role of the oxygen states in many physical properties of 3d perovskites.

2.2. Electric dipole matrix elements

One-electron electric dipole matrix elements for MeO_6 octahedral center can be written with the aid of Wigner–Eckart theorem [36] as follows (see Ref. 34 for details)

$$\langle \gamma_u \mu | \hat{d}_q | \gamma_g \mu' \rangle = (-1)^{j(\gamma_u)-\mu} \begin{pmatrix} \gamma_u & t_{1u} & \gamma_g \\ -\mu & q & \mu' \end{pmatrix}^{*} \langle \gamma_u \| \hat{d} \| \gamma_g \rangle, \tag{3}$$

where $\begin{pmatrix} \cdot & \cdot & \cdot \\ \cdot & \cdot & \cdot \end{pmatrix}$ is the Wigner coefficient for the cubic point group O_h, $j(\Gamma)$ is the so-called quasimomentum number, $\langle \gamma_u \| \hat{d} \| \gamma_g \rangle$ is the one-electron dipole moment submatrix element. The 3d–2p hybrid structure of the even-parity mo-

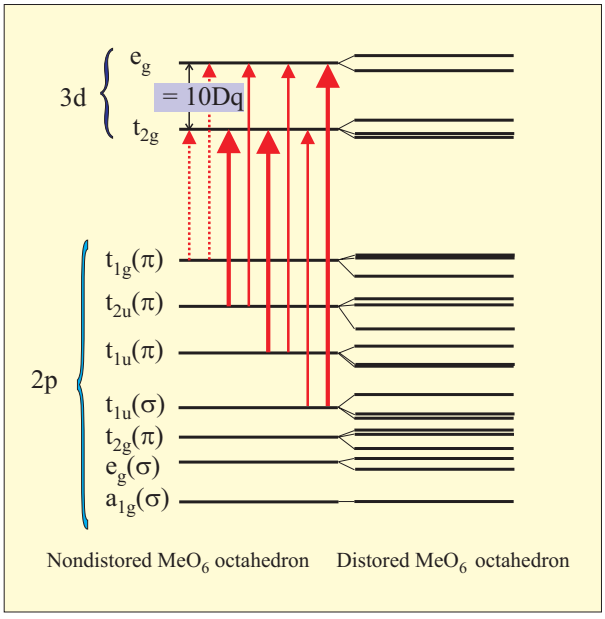

Fig. 1. The diagram of Me3d–O2p molecular orbitals for the MeO_6 octahedral center. The O2p–Me3d charge transfer transitions are shown by arrows: strong dipole-allowed σ–σ and π–π by thick solid arrows; weak dipole-allowed π–σ and σ–π by thin solid arrows; weak dipole-forbidden low-energy transitions by thin dashed arrows, respectively.

lecular orbital $\gamma_g\mu = N_{\gamma_g}(3d\gamma_g\mu + \lambda_{\gamma_g} 2p\gamma_g\mu)$ and a more simple form of purely oxygen odd-parity molecular orbital $\gamma_u\mu \equiv 2p\gamma_u\mu$ both with a symmetry superposition of the ligand O2*p* orbitals point to a complex form of the submatrix element in (3) to be a sum of *local* and *nonlocal* terms composed of the one-site and two-site (*d*–*p* and *p*–*p*) integrals, respectively. In the framework of a simple «local» approximation [34] that implies the full neglect of all many-center integrals

$$\langle t_{2u}(\pi) \| \hat{d} \| e_g \rangle = 0; \quad \langle t_{2u}(\pi) \| \hat{d} \| t_{2g} \rangle = -i\sqrt{\frac{3}{2}}\lambda_\pi d;$$

$$\langle t_{1u}(\sigma) \| \hat{d} \| t_{2g} \rangle = 0; \quad \langle t_{1u}(\sigma) \| \hat{d} \| e_g \rangle = -\frac{2}{\sqrt{3}}\lambda_\sigma d;$$

$$\langle t_{1u}(\pi) \| \hat{d} \| e_g \rangle = 0; \quad \langle t_{1u}(\pi) \| \hat{d} \| t_{2g} \rangle = \sqrt{\frac{3}{2}}\lambda_\pi d. \quad (4)$$

Here, $\lambda_\sigma \sim t_{pd\sigma}/\Delta_{pd}$, $\lambda_\pi \sim t_{pd\pi}/\Delta_{pd}$ are *effective* covalency parameters for e_g, t_{2g} electrons, respectively, $d = eR_0$ is an elementary dipole moment for the cation-anion bond length R_0. We see, that the «local» approximation results in an additional selection rule: it forbids the $\sigma \to \pi$, and $\pi \to \sigma$ transitions, $t_{1u}(\sigma) \to t_{2g}$, and $t_{1,2u}(\pi) \to e_g$, respectively, though these are dipole-allowed. In other words, in frames of this approximation only σ-type ($t_{1u}(\sigma) \to e_g$) or π-type ($t_{1,2u}(\pi) \to t_{2g}$) CT transitions are allowed. Hereafter, we make use of the terminology of «strong» and «weak» transitions for the dipole-allowed CT transitions going on the σ–σ, π–π, and π–σ, σ–π channels, respectively. It should be emphasized that the «local» approximation, if non-zero, is believed to provide a leading contribution to transition matrix elements with corrections being of the first order in the cation-anion overlap integral. Moreover, the nonlocal terms are neglected in standard Hubbard-like approaches. In Fig. 2 we do demonstrate the results of numerical calculations of several two-site dipole matrix elements against 3*d* metal–oxygen separation R_{MeO}. It is clearly seen that given typical cation-anion separations $R_{MeO} \approx 4$ a.u. we arrive at values less than 0.1 a.u. even for the largest two-site integral, however, their neglect should be made carefully. Equations (3), (4) point to likely extremely large dipole matrix elements and oscillator strengths for strong *p*–*d* CT transitions, mounting to $d_{ij} \sim e$Å and $f \sim 0.1$, respectively.

2.3. One-center p–d CT transitions in orthorhombic perovskite manganites

Now we can apply the model theory to the undoped stoichiometric perovskite manganites $RMnO_3$ with MnO_6 octahedra. *Conventional* electronic structure of octahedral MnO_6 complexes is related with the configuration of the completely filled O2*p* shells and partly filled Mn3*d* shells. The typical high-spin ground state configuration and crystalline term for the Mn^{3+} ion in octahedral crystal field or

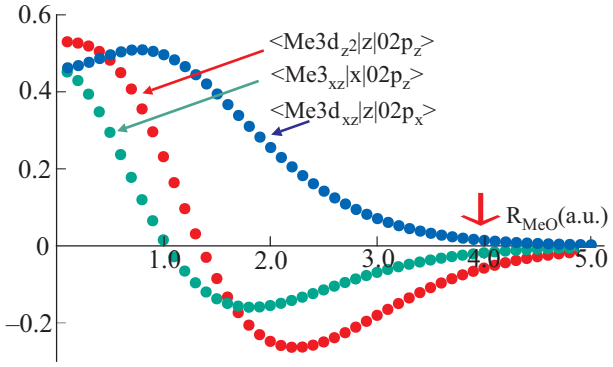

Fig. 2. Two-site dipole matrix elements as a function of Me3*d*–O2*p* separation. The arrow near 4 a.u. points to typical Me3*d*–O separations. For illustration we choose both relatively large integrals $\langle 3d_{z^2} \mid z \mid 2p_z \rangle$ governed by the Me3*d*–O2*p* σ-bond and the relatively small ones $\langle 3d_{xz} \mid z \mid 2p_x \rangle$ and $\langle 3d_{xz} \mid x \mid 2p_z \rangle$ governed by the Me3*d*–O2*p* π-bond. We make use of hydrogen-like radial wave functions with the Clementi–Raimondi effective charges [37] $Z^{\text{eff}}_{\text{O2}p} = 4.45$ and $Z^{\text{eff}}_{\text{Me3}d} = 10.53$ typical for the Mn^{3+} ion.

for the octahedral MnO_6^{9-} center is $t_{2g}^3 e_g^1$ and ^5E_g, respectively. Namely this orbital doublet results in a vibronic coupling and the Jahn–Teller (JT) effect for the MnO_6^{9-} centers, and cooperative JT ordering in $LaMnO_3$. In the framework of a crystal field model the term ^5E_g originates from the $(3d^4)^5D$ term of the free Mn^{3+} ion.

Unconventional electronic configuration of octahedral MnO_6 complexes is related with a *charge transfer state* with one hole in the O2*p* shells [38]. The excited CT configuration $\underline{\gamma}^1_{2p}\ 3d^{n+1}$ arises from the transition of an electron from the MO predominantly anionic in nature (the γ_{2p} hole in the core of the anionic MO being hereby produced), into an empty 3*d* type MO (t_{2g} or e_g). The transition between the ground and the excited configuration can be presented as the $\gamma_{2p} \to 3d(t_{2g}, e_g)$ CT transition.

The CT configuration consists of two partly filled subshells, the ligand γ_{2p} and the cation $3d(t_{2g}^{n_1} e_g^{n_2})$ shell, respectively. The latter configuration in the case of CT states in the MnO_6^{9-} center nominally corresponds to the Mn^{2+} ion. It should be emphasized that the oxygen hole having occupied the *nonbonding* γ_{2p} orbital does interact *ferromagnetically* with the $3d(t_{2g}^{n_1} e_g^{n_2})$ shell. This rather strong ferromagnetic coupling results in the Hund rule for the CT configurations with the high-spin ground states. The maximal value of the total spin for the Hund-like CT state in the MnO_6^{9-} center equals $S = 3$, that points to some perspectives of unconventional magnetic signatures of these states.

For our analysis to be more quantitative we make two rather obvious model approximations. First of all, we assume that for the MnO_6^{9-} centers in $RMnO_3$ as usually for cation-anion octahedra in 3*d* oxides [32,33,35] the nonbonding $t_{1g}(\pi)$ oxygen orbital has the highest energy and forms the first electron removal oxygen state. Furthermore, to be definite we assume that the energy spectrum of the nonbonding oxygen states for $Mn^{3+}O_6^{9-}$ centers in $RMnO_3$ coincides with that calculated in Ref. 35 for $Fe^{3+}O_6^{9-}$ in isostructural orthoferrite $LaFeO_3$, in other words, we have (in eV):

$$\Delta(t_{1g}(\pi)-t_{2u}(\pi))\approx 0.8;\ \Delta(t_{1g}(\pi)-t_{1u}(\pi))\approx 1.8;$$

$$\Delta(t_{1g}(\pi)-t_{1u}(\sigma))\approx 3.0.$$

Secondly, we choose for the Racah parameters B = 12 eV and C = 0.41 eV, the numerical values typical for the Mn^{2+} ion. The crystal-field parameter Dq = 0.15 eV provides a reasonable explanation of the Mn^{2+} spectra in MnO [39]. This set of parameters is used for the model simulation of the overall *p–d* CT band in $LaMnO_3$ [34]. We argue that the lowest in energy spectral feature observed in $LaMnO_3$ near 1.7 eV (see, e.g., Ref. 40) is related with the onset of the series of the dipole-forbidden *p–d* CT transitions $t_{1g}(\pi)\to e_g, t_{2g}$, rather than with any *d–d* crystal field transition. The energy of this transition was picked out a starting point for assignment of all other *p–d* CT transitions.

Weak dipole-allowed π–σ CT transitions $t_{2u}(\pi)-e_g$ and $t_{1u}(\pi)-e_g$ form more intensive CT bands beginning at higher than the preceding series energies, near 2.5 and 3.5 eV, respectively, in accordance with the magnitude of the $t_{1g}(\pi)-t_{2u}(\pi)$ and $t_{1g}(\pi)-t_{1u}(\pi)$ separations. Actually, the $t_{1u}(\pi)-e_g$ transition has to be more intensive because the $t_{1u}(\pi)$ state is partly hybridized with $t_{1u}(\sigma)$, hence this transition borrows a portion of intensity from the strong dipole-allowed $t_{1u}(\sigma)-e_g$ CT transition.

The latter σ–σ transition forms intensive broad CT band starting from the main ${}^5E_g - {}^6A_{1g}$; ${}^5T_{1u}$ peak at ≈ 4.7 eV and ranging to the ${}^5E_g - {}^4A_{2g}$; ${}^5T_{2u}$ peak at ≈ 10.2 eV with interstitial peaks at ≈ 8.0 eV being the result of the superposition of two transitions ${}^5E_g - {}^4A_{1g}$; ${}^5T_{2u}$ and ${}^5E_g - {}^4E_g$; ${}^5T_u$, and at ≈ 8.8 eV due to another ${}^5E_g - {}^4E_g$; ${}^5T_u$ transition, respectively. Thus, the overall width of the CT bands with final $t_{2g}^3 e_g^2$ configuration occupies a spectral range from 1.7 up to ~10 eV.

Strong dipole-allowed π–π CT transitions $t_{2u}(\pi), t_{1u}(\pi)-t_{2g}$ form two manifolds of equally intensive CT bands shifted with respect to each other by the $t_{2u}(\pi)-t_{1u}(\pi)$ separation (≈ 1.0 eV). In turn, each manifold consists of two triplets of weakly split and equally intensive CT bands associated with ${}^5E_g - {}^4T_{1g}$; ${}^5T_u$ and ${}^5E_g - {}^4T_{2g}$; ${}^5T_u$ transitions, respectively. In accordance with the assignment of crystal-field transitions [39] in $LaMnO_3$ we should expect the low-energy edge of the dipole-allowed π–π CT band starting from ≈ 4.5 eV $(1.7+2.0+$ $+(t_{1g}(\pi)-t_{2u}(\pi)$ separation)). Taking account of strong configuration interaction we should expect the high-energy edge of this band associated with the highest in energy ${}^4T_{2g}$ term of the $3d^5$ configuration to be positioned near ≈ 9.9 eV. In between, in accordance with our scheme of energy levels we predict peaks at 5.2; 5.5; 6.2(×2); 7.2(×2); 7.9; 8.2; 8.3; 8.9 eV. The weak dipole-allowed σ–π transitions occupy the high-energy spectral range from 6.7 to 11.1 eV.

Overall, our analysis shows the multi-band structure of the CT optical response in $LaMnO_3$ with the weak low-energy edge at 1.7 eV, associated with forbidden $t_{1g}(\pi)-e_g$ transition and a series of strong bands in the range of 4.6–10.2 eV starting with composite peak at ~ 4.5–4.7 eV and closing by composite peak at 8–10 eV both resulting from the superposition of strong dipole-allowed π–π and σ–σ CT transitions.

Above we addressed the model energies of the CT transitions. In frames of our model the relative intensities for different dipole-allowed CT transitions are governed by the relative magnitude of different one-electron dipole submatrix elements. We have performed the theoretical simulation of the overall O2*p*–Mn3*d* CT optical band in $LaMnO_3$ generated by dipole-allowed CT transitions in MnO_6^{9-} octahedra given simple physically reasonable assumptions concerning the one-electron submatrix elements. We have assumed i) the equal integral intensities $I_{\sigma\sigma}=I_{\pi\pi}$ for the σ–σ and π–π channels, that corresponds to $\lambda_\sigma^2 = 6\lambda_\pi^2$; and ii) the equal integral intensities $I_{\pi\sigma}=I_{\sigma\pi}=0.1I_{\sigma\sigma}$ for all weak dipole-allowed transitions $t_{2u}(\pi)-e_g$, $t_{1u}(\pi)-e_g$, and $t_{1u}(\sigma)-t_{2g}$. The former assumption agrees with the well-known semi-empirical rule that simply states $\lambda_\sigma \sim 2\lambda_\pi$. The latter assumption concerns the outgoing beyond the «local» approximation and seems to be more speculative. Probably, this yields an overestimation for $t_{2u}(\pi)-e_g$ transition, but underestimation for $t_{1u}(\pi)-e_g$ and $t_{1u}(\sigma)-t_{2g}$ transitions, which intensity can be enhanced due to $t_{1u}(\pi)-t_{1u}(\sigma)$ hybridization. The more detailed quantitative description of the weak dipole-allowed CT transitions needs the substantial expansion of our model approach and further theoretical studies.

The calculated model contributions of the dipole-allowed CT transitions to the imaginary part of the dielectric function are presented in Fig. 3. The top panel shows the partial contributions of different dipole-allowed transitions modeled by rather narrow Lorentzians with linewidth Γ = 0.5 eV to clearly reveal the multiplet structure. The lower panel presents the overall contribution to the imaginary part of dielectric function of the dipole-allowed CT transitions. Here, the Lorentzian linewidth is assumed to be $\Gamma = 1.0$ eV for all contributions to maximally reproduce the experimental situation. All the spectra are presented given the same relative units.

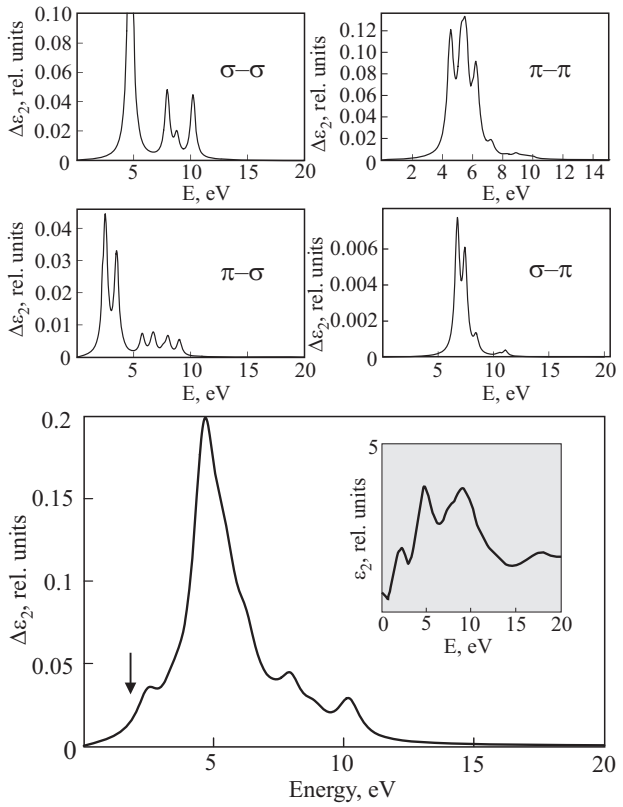

Fig. 3. Theoretical simulation of the overall O2*p*–Mn3*d* CT band in $LaMnO_3$. Top panel shows the partial contributions of different dipole-allowed transitions. Bottom panel presents the overall contribution of the dipole-allowed CT transitions to the imaginary part of dielectric function. Experimental spectrum from the paper by Okimoto *et al.* [41] is shown in insert (see text for details).

In conclusion one should emphasize several points. First, the *p–d* CT excitons can move over the lattice thus forming an excitonic band. Its width would strongly depend on the character of the O2*p* hole state. We anticipate rather narrow bands for π–π and π–σ excitons, but rather wide bands for σ–σ and σ–π excitons. It is worth noting that besides the charge transfer the *p–d* CT transitions in MnO_6 octahedra are characterized by a remarkable effect of the transfer of the spin density and orbital degeneracy from Mn ion to surrounding oxygen ions. In addition, we would like to underline a crucial role of the intra-atomic correlations in forming the optical response in 3*d* oxides. Indeed, the one-electron energy level scheme (see Fig. 1) points to a low-lying $3d\,t_{2g}$ orbital to be a final state for any lower-energy CT transition, while actually the lower-energy CT transitions are related with $3d\,e_g$ orbital as a final state because of a prevailing gain in the Hund energy.

2.4. Role of the Jahn–Teller distortions for the $Mn^{3+}O_6$ *octahedra and the light polarization effects*

Orthorhombic manganites $RMnO_3$ are typical compounds with the 3*d*-electron orbitally ordered ground state where $3d_{3x^2-r^2}$-type and $3d_{3y^2-r^2}$-type orbitals for e_g-electrons are alternately ordered on Mn^{3+} sites in the *ab* plane and are stacked parallel along the *c* axis below the orbital ordering temperature $T_{JT} \sim 750$–1500 K [42]. Such an orbital ordering is stabilized by the cooperative Jahn–Teller effect that lifts the orbital degeneracy of the crystal ground state ^5E term for the octahedral $t_{2g}^3 e_g^2$ electronic configuration of the Mn^{3+} ion. The orbital ordering causes a layer-type (so called *A*-type) antiferromagnetic (AF) ordering below T_N, in which magnetic moments on Mn sites are aligned ferromagnetically in the *ab* plane and are stacked antiferromagnetically along the *c* axis.

The e_g-electron in the JT-distorted $Mn^{3+}O_6$ octahedral cluster occupies the superposition state

$$\Psi_g = \cos\frac{\Theta}{2}\,|\,d_{z^2}\rangle + \sin\frac{\Theta}{2}\,|\,d_{x^2-y^2}\rangle, \qquad (5)$$

where the orbital mixing angle Θ is determined by the deformations of the $Mn^{3+}O_6$ octahedral cluster as follows:

$$\tan\Theta = \frac{\sqrt{3}(l_x - l_y)}{2l_z - l_x - l_y}, \qquad (6)$$

where $l_{x,y,z}$ are the lengths of the Me–O bonds along the respective local co-ordinates. The unoccupied, or e_g-hole state of the same $Mn^{3+}O_6$ octahedral cluster is described by the wave function Ψ_e which is orthogonal to Ψ_g:

$$\Psi_e = -\sin\frac{\Theta}{2}\,|\,d_{z^2}\rangle + \cos\frac{\Theta}{2}\,|\,d_{x^2-y^2}\rangle. \qquad (7)$$

The Jahn–Teller splitting energy is determined as $\Delta_{JT} = 2g\rho_0$, where g is a vibronic constant,

$$\rho_0 = \left[2(l_x - l_y)^2 + 6(l_z - l)^2\right]^{1/2}, \qquad (8)$$

and l is a mean Mn–O bond length. For rare-earth orthorhombic manganites the $Mn–O_I$ bond corresponds to the medium length while two $Mn–O_{II}$ bonds correspond to long and short lengths (see Ref. 42). If the local *z* axis is directed along the $Mn–O_I$ bond and the *x* axis along the $Mn–O_{II}$ bond with the longest length, then $(l_x - l) \gg (l_z - l) \approx (l_y - l)$ and $\tan\Theta \approx \sqrt{3}$, or $\Theta \approx 120^\circ$. In other words, it means that $\Psi_g \approx |\,d_{x^2}\rangle$. In the tetragonal limit ($(l_x - l) \gg (l_z - l) = (l_y - l)$) the e_g level splits into two singlets ($|\,d_{x^2}\rangle$ and $|\,d_{y^2-z^2}\rangle$, respectively), while the t_1, t_2 levels split into singlets and doublets (see Fig. 1). Thus all the one-center *p–d* CT transitions $t_{1,2} \to e_g$ from filled nonbonding oxygen orbitals to empty e_g orbital, both allowed and forbidden, are believed to reveal a singlet-(quasi)doublet structure. The intensity of weakly dipole allowed $t_{2u}(\pi) \to e_g$ transitions centered near 2.5 eV, can

be enhanced due to a $t_{2u}(\pi)-t_{1u}(\pi), t_{1u}(\sigma)$ mixing resulting from the low-symmetry distortions of MnO_6 octahedra.

Let us address the polarization properties of the main dipole-allowed one-center *p–d* CT transition $t_{1u}(\sigma)\to e_g$. To this end we find the dipole transition matrix elements in the local coordinates of the MnO_6 octahedron:

$$\langle t_{1ux}(\sigma)\,|\,d_x\,|\,d_{z^2}\rangle = \langle t_{1uy}(\sigma)\,|\,d_y\,|\,d_{z^2}\rangle =$$

$$= -\frac{1}{2}\langle t_{1uz}(\sigma)\,|\,d_z\,|\,d_{z^2}\rangle = -\frac{\lambda_\sigma d}{\sqrt{6}};$$

$$\langle t_{1ux}(\sigma)\,|\,d_x\,|\,d_{x^2-y^2}\rangle = -\langle t_{1uy}(\sigma)\,|\,d_y\,|\,d_{x^2-y^2}\rangle = \frac{\lambda_\sigma d}{\sqrt{2}} \tag{9}$$

and

$$\langle t_{1ux}(\sigma)\,|\,d_x\,|\,\Psi_e\rangle = \frac{\lambda_\sigma d}{\sqrt{6}}(\sin\frac{\Theta}{2}+\sqrt{3}\cos\frac{\Theta}{2});$$

$$\langle t_{1uy}(\sigma)\,|\,d_y\,|\,\Psi_e\rangle = \frac{\lambda_\sigma d}{\sqrt{6}}(\sin\frac{\Theta}{2}-\sqrt{3}\cos\frac{\Theta}{2});$$

$$\langle t_{1uz}(\sigma)\,|\,d_z\,|\,\Psi_e\rangle = -\frac{2\lambda_\sigma d}{\sqrt{6}}\sin\frac{\Theta}{2}. \tag{10}$$

Hence for spectral weights we obtain the relation as follows:

$$SW_x : SW_y : SW_z =$$

$$= (2+3\sin\Theta+\cos\Theta) : (2-3\sin\Theta+\cos\Theta) : 2(1-\cos\Theta). \tag{11}$$

Neglecting the tilting of the MnO_6 octahedra we arrive at the ratio of spectral weights SW_c and SW_{ab} for light polarized $\|$ *c* axis and $\|$ *ab* plane, respectively [43]:

$$SW_c / SW_{ab} = \frac{2(1-\cos\Theta)}{(2+\cos\Theta)}. \tag{12}$$

Generally speaking, the CT exciton creation is accompanied by an excitation of lattice modes. Indeed, the electron transfer from O $2p$ to Mn $3d$ state, or from an *ionic* to a *covalent* configuration such as σ–σ transition ${}^5\mathrm{E}_g - {}^6A_{1g}$; ${}^5T_{1u}$ is accompanied by a significant shortening of the equilibrium Mn–O bond length and a remarkable effect of the transfer of orbital degeneracy from Mn ion to surrounding oxygen ions accompanied by a strong change in the electron-lattice coupling. Thus, the incident photon can create a self-trapped exciton which can reemit a photon, returning either to the ground state or to various one-phonon or multiphonon excited states. The exciton–phonon interaction strongly affects the line-shape of absorption leading to Franck–Condon multiphonon sidebands and results in a phonon Raman scattering. The measurement of the Raman intensity as a function of excitation light energy is a very informative probe of the origin of electronic transitions.

2.5. One-center p–d CT transitions in perovskite ferrites

The *conventional* ground state electronic structure of octahedral $Fe^{3+}O_6$ complexes is associated with the configuration of the completely filled O2*p* shells and half-filled Fe3*d* shell. The typical high-spin ground state configuration and crystalline term for Fe^{3+} in the octahedral crystal field or for the octahedral $[FeO_6]^{9-}$ center is $t_{2g}^3 e_g^2$ and ${}^6A_{1g}$, respectively.

The conventional classification scheme of the CT transitions in the octahedral FeO_6^{9-} centers (intra-center CT transitions) includes the electric-dipole allowed transitions from the odd-parity oxygen $\gamma_u = t_{1u}(\pi), t_{2u}(\pi), t_{1u}(\sigma)$ orbitals to the even-parity iron $3dt_{2g}$ and $3de_g$ orbitals, respectively. These one-electron transitions generate the many-electron ones ${}^6A_{1g}\to{}^6T_{1u}$, which differ by the crystalline term of the respective $3d^6$ configuration:

$$(t_{2g}^3\,{}^4A_{2g}; e_g^2)^6 A_{1g} \to ((t_{2g}^4; e_g^2)^5 T_{2g}; \underline{\gamma_u})^6 T_{1u}, \tag{13}$$

$$(t_{2g}^3\,{}^4A_{2g}; e_g^2)^6 A_{1g} \to ((t_{2g}^3; e_g^3)^5 E_g; \underline{\gamma_u})^6 T_{1u}, \tag{14}$$

for $\gamma_u \to 3dt_{2g}$ and $\gamma_u \to 3de_g$ transitions, respectively. We see that in contrast to the manganese centers $Mn^{3+}O_6^{9-}$ each one-electron $\gamma_u \to 3dt_{2g}$ transition generates one many-electron CT transition [34].

Hence, starting with three nonbonding purely oxygen orbitals $t_{1u}(\pi), t_{1u}(\sigma), t_{2u}(\pi)$ as initial states for one-electron CT, we arrive at six many-electron dipole-allowed CT transitions ${}^6A_{1g}\to{}^6T_{1u}$. There are two transitions $t_{1u}(\pi), t_{2u}(\pi)\to t_{2g}$ (π–π channel), two transitions $t_{1u}(\pi), t_{2u}(\pi)\to e_g$ (π–σ channel), one transition $t_{1u}(\sigma)\to t_{2g}$ (σ–π channel), and one transition $t_{1u}(\sigma)\to e_g$ (σ–σ channel). In addition, one should account for a dipole-forbidden $t_{1g}(\pi)\to t_{2g}$ transition which determines the onset energy of the CT bands.

The transfer energy in the $Fe^{3+}O_6$ octahedra for the dipole-forbidden $t_{1g}(\pi)-t_{2g}$ transition which determines the onset energy of the *p–d* CT bands can be compared with a similar quantity for the dipole-forbidden $t_{1g}(\pi)-e_g$ transition which determines the onset energy of the *p–d* CT bands in $Mn^{3+}O_6$ octahedra in, e.g., manganite $LaMnO_3$

$$\Delta^{\mathrm{Fe}}_{t_{1g}(\pi)-t_{2g}} - \Delta^{\mathrm{Mn}}_{t_{1g}(\pi)-e_g} =$$

$$= A + 28B - 10Dq - \Delta_{JT} + I_3(\mathrm{Fe}) - I_3(\mathrm{Mn}).$$

Here we made use of the standard Racah parameters, $I_3(\mathrm{Fe}), I_3(\mathrm{Mn})$ are the third ionization potentials for iron and manganese atoms, respectively, Δ_{JT} is the Jahn–Teller splitting of the e_g level in manganite. Given $A \approx 2.0$ eV (see below), $B \approx 0.1$ eV, $Dq \approx 0.1$ eV, $\Delta_{JT} \approx 0.7$ eV, $(I_3(\mathrm{Fe}) - I_3(\mathrm{Mn})) \approx -3.0$ eV (see, e.g., Ref. 44) we get

$\Delta^{\mathrm{Fe}}_{t_{1g}(\pi)-t_{2g}} - \Delta^{\mathrm{Mn}}_{t_{1g}(\pi)-e_g} \approx 1.0$ eV. In other words, the onset of *p–d* CT transitions in the $Fe^{3+}O_6$ octahedra is expected to be noticeably by ~ 1 eV blue-shifted as compared to its $Mn^{3+}O_6$ counterpart. Taking into account $\Delta^{\mathrm{Mn}}_{t_{1g}(\pi)-e_g} \approx 1.7$ eV as the onset energy of *p–d* CT transitions in the $Mn^{3+}O_6$ octahedra in an idealized orthomanganite $LaMnO_3$ [34], we get $\Delta^{\mathrm{Fe}}_{t_{1g}(\pi)-t_{2g}} \approx 2.7$ eV as an estimate of the onset energy of *p–d* CT transitions in the $Fe^{3+}O_6$ octahedra in the isostructural orthoferrite $LaFeO_3$. It is interesting that this low-energy *p–d* CT transition in ferrites can be superimposed on the *d–d* crystal field transitions, in particular, on the ${}^6A_{1g} \to {}^4A_{1g}$ transition usually an important optical signature of the Fe^{3+} centers. Indeed, its energy $\Delta E = 10B + 5C \approx 2.5$–$2.8$ eV does not depend on the crystal field splitting parameter *Dq*, that makes the energy of this transition insensitive to details of the crystalline surroundings. By contrast, both the energy and the intensity of the $t_{1g}(\pi)-t_{2g}$ *p–d* CT transition are strongly dependent on the crystalline surroundings. Being nominally dipole-forbidden for ideal $Fe^{3+}O_6$ octahedra, this transition becomes allowed for noncentrosymmetric $Fe^{3+}O_6$ complexes with a spectral weight typical for CT transitions. In contrast to the ${}^6A_{1g} \to {}^4A_{1g}$ transition, the low-symmetry distortions of $Fe^{3+}O_6$ octahedra give rise to a sizeable splitting of the $t_{1g}(\pi)-t_{2g}$ band that may be used for the transition assignment.

As it was noted above, the onset energy for the *p–d* CT transitions in ferrites is blue-shifted by 1 eV as compared to manganites. However, the low-energy strong dipole-allowed *p–d* CT transitions in ferrites and manganites are anticipated at ~3 and ~4.5 eV, respectively. Such a counter-intuitive picture points to the importance of correlation effects governing the electronic structure in the ground and excited CT states.

2.6. Temperature dependence of the spectral weight for the p–d CT bands

Addressing the temperature dependence of the spectral weight for the *p–d* CT transitions we will first concern the effects of a magnetic ordering. At first sight for small one-center excitons we have a rather conventional transition with conservation of spin SM_S-state and a spin density fluctuation localized inside the MeO_6 cluster. However, the redistribution of the spin density from 3*d* atom to the oxygen ones after the *p–d* CT transition switches on a strong ferromagnetic Heisenberg O2*p*–Me3*d* exchange that leads to a number of temperature anomalies near the Néel temperature. At first, one has to expect a blue shift effect for the transition energy with the lowering the temperature near and below T_N. Indeed, at $T > T_N$, the average molecular field for the MeO_6 center turns into zero while the 3*D* antiferromagnetic ordering is accompanied by a rise of the exchange molecular fields and respective spin splittings. Due to an order of magnitude bigger value of the O2*p*–Me3*d* exchange as compared with the Me3*d*–Me3*d* exchange this is accompanied by an increase of the transition energy with a maximal value of the blue shift as large as several tenths of eV. Additionally, one has to expect a strong (of the same order of magnitude) broadening of the excitonic line with the increase of the temperature due to strong fluctuations of molecular fields.

The temperature dependence of the phonon-assisted *p–d* CT transitions, such as $t_{1g}(\pi) \to e_g, t_{2g}$, normally forbidden by parity considerations, is usually described by the functional form predicted for such a type of process:

$$SW(T) = SW(0)\coth\frac{\hbar\omega_p}{2kT},$$

where $SW(0)$, the spectral weight at 0 K, embodies the effect of parity mixing introduced by lattice vibrations in the states connected by the transition, and $\hbar\omega_p$ is a phonon energy. Depending on the energy of the active odd-parity phonon mode(s) such a mechanism can provide up to a twofold rise of the spectral weight with the temperature rise from helium to room temperatures. Obviously, this transition borrows a portion of intensity from the nearest in the energy dipole-allowed CT transitions.

It should be noted that equally with the band-structure effects the electron–phonon interaction governs the line-shape and the temperature dependence of all the CT transitions, both dipole-allowed and dipole-forbidden.

3. Two-center *d–d* CT transitions

Inter-center *d–d* CT transitions between two MeO_n clusters centered at neighboring sites 1 and 2 define two-center *d–d* CT excitons in 3*d* oxides. These two-center excitons may be addressed as quanta of the disproportionation reaction

$$\mathrm{Me_1O_n^v} + \mathrm{Me_2O_n^v} \to \mathrm{Me_1O_n^{v-1}} + \mathrm{Me_2O_n^{v+1}}, \qquad (15)$$

with the creation of electron MeO_n^{v-1} and hole MeO_n^{v+1} centers. Depending on the initial and final single particle states all the intersite *d–d* CT transitions may be classified to the e_g-e_g, e_g-t_{2g}, $t_{2g}-e_g$, and $t_{2g}-t_{2g}$ ones. For the 3*d* oxides with cations obeying the Hund rule these can be divided to so-called high-spin (HS) transitions $S_1S_2S \to S_1 \pm \frac{1}{2}S_2 \mp \frac{1}{2}S$ and low-spin (LS) transitions $S_1S_2S \to S_1 - \frac{1}{2}S_2 - \frac{1}{2}S$, respectively.

3.1. Effect of orbital states and Me_1–O–Me_2 *bond geometry*

The dipole matrix element for the $\gamma_1 \to \gamma_2$ transition between the even-parity ground state Ψ^g_{GS} and the odd-parity excited state Ψ^u_{ES} of the Me_1–Me_2 pair can be ex-

pressed through the transfer integral t_{12} and the transfer energy Δ_{12} as follows

$$\langle \Psi^g_{GS} \,|\, \hat{\mathbf{d}} \,|\, \Psi^u_{ES} \rangle \approx 2e\mathbf{R}_{12} \frac{t_{12}}{\Delta_{12}}. \qquad (16)$$

In other words, the spectral weight of the two-center *d–d* CT transition can be related to the kinetic contribution $J_{\rm kin} = t_{12}^2 / \Delta_{12}$ to the exchange integral in the 12 pair [45].

The transfer integrals in 3*d* oxides can strongly depend on the bond geometry. For two octahedral MeO_6 clusters sharing a common oxygen ion we get the following expressions for the transfer integrals:

$$t_{12}(e_g 0; e_g 0) \approx t_{ss} + t_{\sigma\sigma} \cos\theta;$$

$$t_{12}(e_g 0; e_g 2) = t_{12}(e_g 2; e_g 0) = t_{12}(e_g 2; e_g 2) = 0;$$

$$t_{12}(e_g 0; t_{2g}\mu) \approx t_{\sigma\pi} D^{(1)}_{0\mu}(\omega);\; t_{12}(t_{2g}\mu; e_g 0) \approx t_{\pi\sigma} D^{(1)}_{\mu 0}(\omega);$$

$$t_{12}(t_{2g}\mu_1; t_{2g}\mu_2) \approx t_{\pi\pi} D^{(1)}_{\mu_1\mu_2}(\omega), \qquad (17)$$

where the 3*d* orbitals $e_g\mu$ ($e_g 0 = d_{z^2}, e_g 2 = d_{x^2-y^2}$), $t_{2g}\mu$ ($t_{2g}\pm 1 = \mp\frac{1}{\sqrt{2}}(d_{xz} \pm i d_{yz})$, $t_{2g} 2 = d_{xy}$) are specified in the local co-ordinates for Me_1O_6 and Me_2O_6 clusters with z_1 and z_2 axes directed to the common oxygen ion; $t_{\alpha\beta}$ are transfer parameters for $\alpha(\beta) = s, \sigma, \pi$ bonds, respectively; θ is the Me_1–O–Me_2 bond angle; $D^{(1)}_{\mu_1\mu_2}(\omega)$ is the Wigner rotation matrix [36] with ω being the Euler angles, specifying the transformation from the local co-ordinates for Me_1O_6 o those for the Me_2O_6 cluster. These expressions can be used to find a detailed relation between bond geometry and the spectral weight of the *d–d* CT transitions.

3.2. Role of spin correlations

After uncovering the role of the Me_1–O–Me_2 bond angle, we have to consider whether the spin degree of freedom affects the *d–d* CT transition. It should be noted that despite the spinless character of the dipole moment operator its matrix elements on the pair wave functions depend on the spin quantum numbers. In particular, the partial spectral weight (SW) for a $S_1S_2 \to S_1'S_2'$ transition can be given as follows:

$$SW(S_1S_2 \to S_1'S_2') \propto [S_1, S_2'] \sum_S \rho_S \begin{Bmatrix} S_1 & S_2 & S \\ S_2' & S_1' & \frac{1}{2} \end{Bmatrix}^2, \qquad (18)$$

where ρ_S is the temperature-dependent statistical weight of the S_1S_2S spin multiplet, $\begin{Bmatrix} S_1 & S_2 & S \\ S_2' & S_1' & \frac{1}{2} \end{Bmatrix}$ is the 6*j*-symbol [36]. Taking into account the expressions for 6*j*-symbols we see that the temperature dependence of the partial spectral weight $SW(S_1S_2 \to S_1'S_2')$ should be determined by a statistical average $\langle S(S+1)\rangle = \langle \hat{\mathbf{S}}^2 \rangle$ which, in its turn, relates to the spin-spin correlation function $\left\langle \left(\hat{\mathbf{S}}_1 \cdot \hat{\mathbf{S}}_2 \right) \right\rangle$. Thus we should conclude that the partial spectral weight for $S_1S_2S \to S_1'S_2'S$ transitions in an isolated spin pair is governed by a spin-dependent prefactor containing the spin–spin correlation function $\left\langle \left(\hat{\mathbf{S}}_1 \cdot \hat{\mathbf{S}}_2 \right) \right\rangle$. For the HS transition $S_1S_1 \to S_1 - \frac{1}{2} S_1 + \frac{1}{2}$ and the LS transition $S_1S_1 \to S_1 - \frac{1}{2} S_1 - \frac{1}{2}$ in the pair of identical 3*d* ions one gets

$$SW(S_1S_1 \to S_1 - \frac{1}{2} S_1 + \frac{1}{2}) \propto$$

$$\propto \frac{\langle S(S+1)\rangle}{2S_1(2S_1+1)} = \frac{\left[\left\langle \left(\hat{\mathbf{S}}_1 \cdot \hat{\mathbf{S}}_2 \right) \right\rangle + S_1(S_1+1) \right]}{S_1(2S_1+1)}, \qquad (19)$$

$$SW(S_1S_1 \to S_1 - \frac{1}{2} S_1 - \frac{1}{2}) \propto$$

$$\propto \frac{\left[2S_1(2S_1+1) - \langle S(S+1)\rangle \right]}{2S_1(2S_1+1)} = \frac{\left[S_1^2 - \left\langle \left(\hat{\mathbf{S}}_1 \cdot \hat{\mathbf{S}}_2 \right) \right\rangle \right]}{S_1(2S_1+1)}, \qquad (20)$$

respectively. These expressions allow one to obtain both the low-temperature ($T \ll T_N$) and high-temperature ($T \gg T_N$, $\left(\hat{\mathbf{S}}_i \cdot \hat{\mathbf{S}}_j \right) \to 0$) limits for the spin prefactor. In accordance with a spin sum rule the sum of spin prefactors on the right hand sides of the expressions (19) and (20) turns into unity due to the exact compensation of temperature dependent terms with the spin-spin correlation function. In other words, the higher-energy LS bands exhibit a strictly inverse SW evolution with temperature as compared to the HS band. Varying the temperature we get the SW transfer between the HS- and the LS-subbands. It should be noted that for the Fe^{3+} ion based oxides we deal only with the LS-transitions $\frac{5}{2}\frac{5}{2} \to 22$ and the antiferromagnetic ground state exchange coupling.

3.3. Some features of CT transitions in strongly coupled corner-shared MeO_6 *clusters*

Above we have addressed a somewhat idealized scenario of *p–d* and *d–d* CT transitions which implies well isolated or weakly coupled MeO_6 clusters. Actually in perovskite manganites and ferrites we deal with strongly coupled corner-shared MeO_6 clusters sharing a common oxygen ion. Strictly speaking, it means that we cannot make use of an oversimplified classification of the *p–d* and *d–d* CT transitions. Indeed, the O2*p* electrons localized on the intermediate common oxygen ion cannot be attributed to one or another cluster. Formally this implies a strong overlap of the bare wave functions localized on the neigh-

boring clusters. Generally speaking, this trouble can be overcome with making use of the orthogonalization procedure. This immediately results in a two-center character of the wave functions with the onset of two-center spin and orbital correlations.

Many features of the corner-shared MeO_6 clusters related with the *p–d* overlap and covalency effects can be illustrated by a more simple generic two-hole-three-site Me_1–O–Me_2 cluster model. To this end we start with the construction of spin-singlet and spin-triplet wave functions for our three-center two-hole system taking account of the *p–d* hopping, on-site hole-hole repulsion, and crystal field effects for the bare ground state 101 and bare excited configurations $\{n\}$ (011, 110, 020, 200, 002) with different hole occupation of M_1, O, and M_2 sites, respectively. The *p–d* hopping for M–O bond implies a conventional Hamiltonian

$$\hat{H}_{pd} = \sum_{\alpha\beta} t_{p\alpha d\beta} \hat{p}^{\dagger}_{\alpha} \hat{d}_{\beta} + \text{h.c.}, \tag{21}$$

where $\hat{p}^{\dagger}_{\alpha}$ creates a hole in the α state on the oxygen site, while $\hat{d}_{\beta}$ annihilates a hole in the β state on the copper site.

Perturbed wave functions can be written as follows

$$\Psi_{\{n\}\Gamma SM} = \eta^{\Gamma S}_{\{n\}} [\Phi_{\{n\}\Gamma SM} + \sum_{\{n\}' \neq \{n\}, \Gamma'} c^{\{n\}'\Gamma' S}_{\{n\}\Gamma S} \Phi_{\{n\}'\Gamma' SM}], \tag{22}$$

where $\Phi_{\{n\}\Gamma SM}$ are bare wave functions for $\{n\}$ configuration and the summation runs both on different configurations and different orbital Γ states;

$$\eta^{\Gamma S}_{\{n\}} = \left(1 + \sum_{\{n\}' \neq \{n\}, \Gamma'} \left| c^{\{n\}'\Gamma' S}_{\{n\}\Gamma S} \right|^2 \right)^{-1/2} \tag{23}$$

is a normalization factor. If we neglect the overlap integrals, the probability amplitudes for configurations coupled by a single *p–d* transfer are defined by the ratio of the generalized *p–d* transfer integrals and the *p–d* transfer energy as follows:

$$|c^{011}_{101}| \sim |c^{110}_{101}| \sim |c^{110}_{020}| \sim |c^{020}_{110}| \sim |c^{200}_{110}|, \ldots \sim |\frac{t_{pd}}{\Delta_{pd}}|,$$

while the probability amplitudes, or hybridization parameters for configurations coupled by a two-step *p–d* transfer, such as c^{200}_{101}, c^{020}_{101}, c^{002}_{101} are on the order of $|\frac{t_{pd}}{\Delta_{pd}}|^2$.

Formally, the $101 \rightarrow 011(110)$ and $101 \rightarrow 002(200)$ CT transitions may be attributed to *p–d* and *d–d* charge transfer, respectively. However, the configuration interaction due to the charge transfer and overlap do result in that both types of the CT transitions are accompanied by a charge redistribution all over the three centers. Furthermore, a novel type of p^2–*dd* CT transitions $101 \rightarrow 020$ does emerge due to a mixing of all the 101, 110, 011, 020 configurations in the initial and final states. Obviously, the main contributions to dipole transition matrix elements for *p–d*, *d–d*, and p^2–*dd* CT transitions are proportional to

$$\frac{t_{pd}}{\Delta_{pd}}, \ |\frac{t_{pd}}{\Delta_{pd}}|^2, \text{ and } |\frac{t_{pd}}{\Delta_{pd}}|^2,$$

respectively. Accordingly, the spectral weights for the dipole allowed *p–d*, *d–d*, and p^2–*dd* CT transitions are

$$SW_{p-d} \propto \left(\frac{t_{pd}}{\Delta_{pd}}\right)^2; \ SW_{d-d} \propto \left(\frac{t_{pd}}{\Delta_{pd}}\right)^4; \ SW_{p^2-dd} \propto \left(\frac{t_{pd}}{\Delta_{pd}}\right)^4,$$

respectively.

Interestingly, all the dipole-allowed CT transitions obey the $\Delta S = 0$ spin-selection rule, however, the dipole transition matrix elements depend on the total spin *S* due to a spin (S) dependence of the energy denominators in the probability amplitudes and so in the normalization factors, particularly due to a contribution of 200, 020, and 002 two-hole on-site configurations. Indeed, for such configurations the spin-singlet and spin-triplet terms are usually separated by a large energy gap. In general, the spin-dependent part of the electric dipole moment operator acting in the basis of the three-site wave functions can be written as follows

$$\hat{\mathbf{P}}_s = \hat{\mathbf{\Pi}}(\hat{\mathbf{s}}_1 \cdot \hat{\mathbf{s}}_2). \tag{24}$$

Such a spin operator for a transition dipole moment was firstly introduced by Sugano *et al*. [24] to explain so-called magnon side-bands in the optical absorption spectra of magnetic crystals. Simple estimates yield

$$|\mathbf{\Pi}| \propto \left(\frac{t_{pd}}{\Delta_{pd}}\right)^3 \text{ and } |\mathbf{\Pi}| \propto \left(\frac{t_{pd}}{\Delta_{pd}}\right)^2$$

for *p–d* and *d–d* CT transtions, respectively. In other words, the spin-dependent part of the spectral weight for both transitions appears to be of the same order: $SW_{\text{spin}} \propto \left(\frac{t_{pd}}{\Delta_{pd}}\right)^4$. It should be noted that the spin-dependent part of the spectral weight in the three-site two-hole cluster can be written as follows:

$$SW_{\text{spin}} = (SW_{\text{triplet}} - SW_{\text{singlet}})(\hat{\mathbf{s}}_1 \cdot \hat{\mathbf{s}}_2), \tag{25}$$

if to take into account that

$$(\hat{\mathbf{s}}_1 \cdot \hat{\mathbf{s}}_2)^2 = \frac{3}{16} - \frac{1}{2}(\hat{\mathbf{s}}_1 \cdot \hat{\mathbf{s}}_2).$$

From this reasoning we may conclude that, in contrast to a clue point of papers by Kovaleva *et al*. [45,46], the both dipole-allowed *d–d* and *p–d* CT transtions in $RMnO_3$ with corner-shared MnO_6 octahedra are equally sensitive to the temperature-dependent spin correlations, only with a different *relative* change of the optical response through the

onset of the magnetic order, relatively large for the former and relatively small for the latter.

3.4. Two-center d–d CT transitions in manganites

The inter-center *d–d* CT transition in manganites

$$MnO_6^{9-} + MnO_6^{9-} \to MnO_6^{8-} + MnO_6^{10-} \qquad (26)$$

implies the creation of the hole MnO_6^{8-} and electron MnO_6^{10-} centers with electron configurations formally related to Mn^{4+} and Mn^{2+}, respectively. The HS one-particle *d–d* CT transition driven by $e_g - e_g$ transfer can be written as follows:

$$MnO_6^{9-}(t_{2g}^3;{}^4A_{2g}e_g^1;{}^5E_g) + MnO_6^{9-}(t_{2g}^3;{}^4A_{2g}e_g^1;{}^5E_g) \to$$

$$\to MnO_6^{8-}(t_{2g}^3;{}^4A_{2g}) + MnO_6^{10-}(t_{2g}^3;{}^4A_{2g}e_g^2;{}^3A_{2g} : {}^6A_{1g}). \qquad (27)$$

The transition energy Δ for such an anti-Jahn–Teller transition is defined as follows:

$$\Delta = \Delta_{JT} + U_d - V_{dd} \qquad (28)$$

that points to its dependence on the structural parameters (see (8)).

The energies of different *d–d* CT transitions $d^{n_1}d^{n_2} \to d^{n_1-1}d^{n_2+1}$ can be easily derived using the proper Tanabe–Moriya diagrams for the d^{n_1-1} and d^{n_2+1} configurations. For instance, the low-energy HS $d(e_g)-d(e_g)$ CT transition ${}^5E_g{}^5E_g \to {}^4A_{2g}{}^6A_{1g}$ (27) sets up a rather wide band of the LS ${}^5E_g{}^5E_g \to {}^4A_{2g}{}^4\Gamma_2$ $d(e_g)-d(e_g)$ CT transitions $({}^4\Gamma_2 = {}^4A_{1g}, {}^4E_g({}^4G), {}^4E_g({}^4D), A_{2g}({}^4F))$ with the energy separations (given a cubic symmetry):

$$\Delta E({}^4A_{1g}, {}^4E_g({}^4G)) = 10B + 5C;$$

$$\Delta E({}^4E_g({}^4D)) = 17B + 5C;$$

$$\Delta E({}^4A_{2g}({}^4F)) = 22B + 7C,$$

which do not depend on the crystal field splitting parameter Dq and do scarcely vary from one compound to another that makes the transitions to be important optical signatures of the $d(e_g)-d(e_g)$ charge transfer. Making use for the Racah parameters the numerical values typical for free Mn^{2+} ion: B = 0.12; C = 0.41 eV, we arrive at three LS $d(e_g)-d(e_g)$ CT bands separated from the low-energy HS $d(e_g)-d(e_g)$ CT band by 3.2, 4.1, and 5.5 eV, while from experimental optical spectra for MnO [39] we obtain slightly lower energies: 2.8, 3.8, and 5.1 eV, respectively.

It should be noted that the intra-atomic electron-electron repulsion does mix the $t_{2g}^{n_1};{}^{2S_1+1}\Gamma_1 e_g^{n_2};{}^{2S_2+1}\Gamma_2 : {}^{2S+1}\Gamma$ states with different configurations and/or different intermediate momenta $S_{1,2}, \Gamma_{1,2}$ but the same crystal terms ${}^{2S+1}\Gamma$. This point is of a great importance for ${}^4E_g({}^4G)$ and ${}^4E_g({}^4D)$ terms of Mn^{2+} which are a result of the interaction of two bare terms: $t_{2g}^3;\ {}^4A_{2g}e_g^2;{}^1E : {}^4E_g$ and $t_{2g}^3;{}^2Ee_g^2;{}^3A_{2g} : {}^4E_g$, repectively. It is worth noting that only the former $t_{2g}^3;{}^4A_{2g}e_g^2;{}^1E : {}^4E_g$ term is active in the $d(e_g)-d(e_g)$ charge transfer, which does not affect the t_{2g} subshell.

The wave functions for ${}^4E_g({}^4G)$ and ${}^4E_g({}^4D)$ terms can be written as follows:

$$\Psi({}^4E_g({}^4D)) = \cos\alpha\,\Psi({}^4A_{2g};{}^1E_g : {}^4E_g) +$$

$$+ \sin\alpha\,\Psi({}^2E_g;{}^3A_{2g} : {}^4E_g)$$

$$\Psi({}^4E_g({}^4G)) = \sin\alpha\,\Psi({}^4A_{2g};{}^1E_g : {}^4E_g) -$$

$$- \cos\alpha\,\Psi({}^2E_g;{}^3A_{2g} : {}^4E_g), \qquad (29)$$

where $\tan 2\alpha = 4\sqrt{3}$, and $\alpha \approx 41^\circ$. In other words, the both terms are almost equally involved in the $d(e_g)-d(e_g)$ charge transfer under consideration.

In the ≈ 3 eV gap in between the low-energy HS and LS $d(e_g)-d(e_g)$ CT transitions one may observe a relatively weak low-energy HS $d(t_{2g})-d(e_g)$ CT transition ${}^5E_g{}^5E_g \to {}^4T_{2g}{}^6A_{1g}$ at the energy $\Delta + 10Dq$ and low-energy LS $d(t_{2g})-d(e_g)$ CT transitions ${}^5E_g{}^5E_g \to {}^4A_{2g}{}^4T_{1g}$, ${}^4T_{2g}$ anticipated at the energies Δ + 21 eV and $\Delta + 2.4$ eV, respectively [39]. Spectral weights for both transitions are determined by $t_{2g}-e_g$ (e_g-t_{2g}) transfer integrals which are believed to be relatively small as compared with large e_g-e_g transfer integrals.

3.5. Two-center d–d CT transitions in ferrites

A two-center *d–d* CT transition in iron oxides with $Fe^{3+}O_6$ octahedra

$$[FeO_6]^{9-} + [FeO_6]^{9-} \to [FeO_6]^{10-} + [FeO_6]^{8-} \qquad (30)$$

implies the creation of electron $[FeO_6]^{10-}$ and hole $[FeO_6]^{8-}$ centers with electron configurations formally related to Fe^{2+} and Fe^{4+} ions, respectively. Two-center *d–d* CT transitions from the initial $Fe^{3+}O_6(t_{2g}^3e_g^2) : {}^6A_{1g}$ states can be directly assigned to $e_g \to e_g$, $e_g \to t_{2g}$, $t_{2g} \to e_g$, and $t_{2g} \to t_{2g}$ channels with final configurations and terms

$$e_g \to e_g : t_{2g}^3e_g^1;{}^5E_g - t_{2g}^3e_g^3;{}^5E_g,$$

$$e_g \to t_{2g} : t_{2g}^3e_g^1;{}^5E_g - t_{2g}^4e_g^2;{}^5T_{2g},$$

$$t_{2g} \to e_g : t_{2g}^2 e_g^2 ; {}^5T_{2g} - t_{2g}^3 e_g^3 ; {}^5E_g,$$

$$t_{2g} \to t_{2g} : t_{2g}^2 e_g^2 ; {}^5T_{2g} - t_{2g}^4 e_g^2 ; {}^5T_{2g}. \qquad (31)$$

In the framework of high-spin configurations the $e_g \to t_{2g}$, CT transition has the lowest energy $\Delta = \Delta_{e_g - t_{2g}}$, while the $e_g \to e_g$, $t_{2g} \to t_{2g}$, and $t_{2g} \to e_g$, transitions have the energies $\Delta + 10Dq(3d^6)$, $\Delta + 10Dq(3d^4)$, and $\Delta + 10Dq(3d^6) + 10Dq(3d^4)$, respectively. The transfer energy in the Fe^{3+}-based ferrites for the $e_g \to t_{2g}$ CT transition

$$\Delta_{e_g t_{2g}}^{\text{Fe–Fe}} = A + 28B - 10Dq$$

can be compared with a similar quantity for the $e_g \to e_g$ CT transition in Mn^{3+}-based manganite $LaMnO_3$

$$\Delta_{e_g e_g}^{\text{Mn–Mn}} = A - 8B + \Delta_{JT},$$

where Δ_{JT} is the Jahn–Teller splitting of the e_g levels in manganite. Given $B \approx 0.1$ eV, $Dq \approx 0.1$ eV, $\Delta_{JT} \approx 0.7$ eV, $\Delta_{e_g e_g}^{\text{Fe–Fe}} \approx 2.0$ eV (see, e.g., Ref. 45) we get $A \approx 2.0$ eV, $\Delta_{e_g t_{2g}}^{\text{Fe–Fe}} \approx 4.0$ eV. In other words, the onset of the *d–d* CT transitions in Fe^{3+}-based ferrites is strongly (~ 2 eV) blue-shifted as compared to the Mn^{3+}-based manganite $LaMnO_3$.

Another important difference between ferrites and manganites lies in the opposite orbital character of initial and final states for the *d–d* CT transitions. Indeed, the low-energy $d^4 d^4 \to d^3 d^5$ CT transition in manganites implies an orbitally degenerate Jahn–Teller initial state ${}^5E_g {}^5E_g$ and an orbitally nondegenerate final state ${}^4A_{2g} {}^6A_{1g}$ while the low-energy $d^5 d^5 \to d^4 d^6$ CT transitions in ferrites imply an orbitally nondegenerate initial state ${}^6A_{1g} {}^6A_{1g}$ and an orbitally degenerate Jahn–Teller final states such as ${}^5E_g {}^5E_g$ for $e_g \to e_g$ or ${}^5E_g {}^5T_{2g}$ for $e_g \to t_{2g}$ CT transitions. An unconventional final state with an orbital degeneracy on both sites, or Jahn–Teller excited states may be responsible for the complex multi-peak lineshape of the *d–d* CT band in ferrites.

4. Charge transfer spectroscopy of manganites: experimental data and discussion

Manganese oxides on the basis of Mn^{3+} ($3d^4$ state) and Mn^{4+} ($3d^3$ state) ions hold a distinguished position among known multiferroics. Orthorhombic perovskite-type manganites $RMnO_3$ (R = La–Dy) with the Jahn–Teller Mn^{3+} ions and hexagonal manganites $RMnO_3$ (R = Y, Dy–Lu) became the most popular objects for the studies of the gigantic magnetoelectric effect and strong dielectric anomalies at the magnetic phase transitions. A lot of attention have been devoted in the recent years to the orthorhombic mixed-valent Mn^{3+}–Mn^{4+} manganites RMn_2O_5 (R = Tb, Dy, *et al*.) where giant magnetoelectric effects have been also observed. Hereafter, in the Section, we report the results of experimental investigations of optical response for single crystalline samples of manganites aimed to study the CT transitions, optical anisotropy, and uncover electronic states as potential contributors to giant multiferroicity. A discussion of the experimental data has been done in frames of the cluster theory of *p–d* and *d–d* CT transitions.

4.1. Perovskite manganites $RMnO_3$

Virtually all the experimental optical data available for manganites are focused on $LaMnO_3$. Except for paper by Kim *et al*. [47] on the absorption spectroscopy of thin films of $RMnO_3$ (R = La, Pr, Nd, Gd, Tb), there has been no effort to perform a comparative study of the optical response for different rare-earth perovskite manganites. The optical conductivity spectrum of $LaMnO_3$ exhibits two broad intensive bands centered around 2.0 and 4–5 eV [40,41,48,49]. However, it has remained unclear just what the nature of the related electron-hole excitations. Some authors [41,48,49] assign these both features to the dipole-allowed *p–d* CT transitions like $t_{2g}^3 e_g^1 - t_{2g}^3 e_g^2 \underline{L}$ and $t_{2g}^3 e_g^1 - t_{2g}^4 e_g^1 \underline{L}$ ($\underline{L}$ denoting a ligand hole), respectively. However, others [40] assign the low-energy band to the «intra-atomic» ${}^5E_g$–${}^5E_g'$ transition, or doubly-forbidden (parity and orbital quasimomentum) *d–d*-like crystal-field transition between two ${}^5E_g$-sublevels separated by a splitting due to a low-symmetry crystalline field. Both interpretations being particularly qualitative suffer from many shortcomings and give rise to many questions concerning the details of the charge transfer states or expected extremely weak intensity for the *d–d* crystal field transitions. Pronounced temperature rearrangement of the optical spectral weight both for low- and high-energy bands was uncovered by Quijada *et al*. [50]. These authors were seemingly the first who made a valid conclusion that the dominant contribution to the optical spectral weight of the conductivity peak at 2.0 eV is provided by the CT hopping between nearest-neighbor manganese ions, or inter-site *d–d* CT transitions.

First ellipsometry measurements for the single crystalline $LaMnO_3$ samples were performed by Loshkareva *et al*. [51] at room temperature and for the spectral range of 1.0–5.0 eV. Later on the ellipsometry measurements were performed for an untwined crystal of $LaMnO_3$ by Kovaleva *et al*. [45,46] in a wide temperature range. The authors have presented a detailed quantitative analysis of the pronounced redistribution of the spectral weight near the Néel temperature. They concluded that the low-energy optical band around 2 eV consists of three distinct bands all assigned to intersite *d–d* CT transitions, and that $LaMnO_3$ is a Mott–Hubbard rather than a charge transfer *p–d* insulator

as argued earlier (see, e.g., Refs. 34, 43). A similar interpretation of spectral features near 2 eV observed in multiferroic $TbMnO_3$ was reported very recently by Bastjan et al. [52]. Many researchers [43,45,46,53,54] pointed to a fine sub-peak structure of the low-energy 2 eV band. Early optical transmission spectra of the $LaMnO_3$ films [53] revealed a fine structure with two features near 1.7 and 2.4 eV, respectively, which were assigned to the Mn^{3+} d–d crystal-field transition ${}^5E_g - {}^3T_{1g}$, split by the JT effect. Up to this point, there has been little effort to understand this sub-peak structure. Such an ambiguity leaves the question of the nature of the main optical transitions and low-lying electron states in $RMnO_3$ far from being resolved.

Figure 4 shows the ε_1 and ε_2 room temperature spectra of $LaMnO_3$ we measured for light polarization **E** ∥ **a**-axis. The optical spectra are interesting in several aspects. First of all, as in many earlier works on $LaMnO_3$, we clearly see two intensive and rather broad optical features peaked at around 2 and 5 eV, respectively. The broad 2 eV band exhibits strong anisotropy, it is hardly visible at **E** ∥ **c**-axis polarization [45,46,55]. As expected, our measurements together with data for $LaMnO_3$ [45,46,51] and $RMnO_3$ (R = Nd, Pr, Sm, Eu) [55] have uncovered many subtle features missed in earlier optical experiments on parent manganites. First, the comparative analysis of the ε_1 and ε_2 spectra allows us to unambiguously conclude that the 2 eV feature is composed of a single intensive and rather broad band peaked at 2.0 eV for $LaMnO_3$, and several relatively weak and narrow bands peaked nearly equally for all the manganites at 1.3, 1.9, 2.3, 2.7 eV (ε_{ab}), respectively [55]. This observation immediately points to different nature of both features at variance with Kovaleva *et al*. [45] who addressed the 2 eV feature in $LaMnO_3$ to consist of three distinct bands, peaked at 1.95, 2.35, 2.70 (ε_{2ab}, T = = 300 K) each attributed to inter-site d–d CT transitions.

As regards the high energy spectral feature peaked at around 5 eV one should note its hardly visible composite

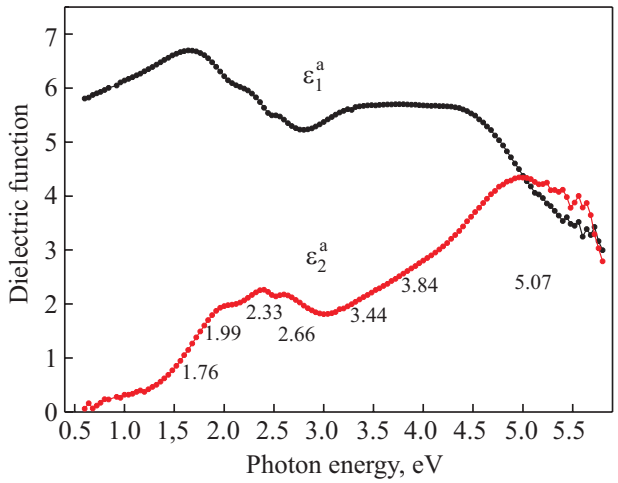

Fig. 4. Spectral dependencies of the real and imaginary parts of the dielectric function ε^{aa} for orthorhombic $LaMnO_3$.

structure with as minimum three rather intensive bands which integral spectral weight for **E** ∥ **c**-axis polarization seems to be slightly larger than for **E** ⊥ **c**-axis polarization.

In Fig. 4 we have presented the results of a semi-quantitative analysis of the spectra in the energy range covered by our experiment based on a dispersion analysis of the complex dielectric function ε, which was fitted by a set of 7 Lorentzian oscillators. It is worth noting, that the Lorentzian fitting should be made with a great care because of several points. First of all, the Lorentzian function is a clear oversimplification for complex line-shapes resulting from an interplay of the electron-lattice interaction and excitonic band effects. Second, it is worth noting the increased uncertainties both of the measurement and, accordingly, of the analysis close to the low- and high-energy cutoffs of our experiment. It should be noted that the results of the Lorentzian fitting for the ε_1 near 2 eV optical feature rather than ε_2 are quite robust to the assumptions related with the transitions beyond the energy range. All the oscillators particularly visible in $RMnO_3$ (R = Nd, Pr, Sm, Eu) [55] can be sorted into three groups assigned to: i) an intensive and broad band peaked at 2.2 eV, ii) weak and narrow bands peaked at 1.3, 1.9, 2.3, 2.65 eV, forming a fine structure of 2 eV band, and iii) intensive bands peaked at 3.0, 3.9, 4.65, 5.3 eV, forming a broad spectral feature peaked at around 4–5 eV. Both the spectral weight, polarization properties, and temperature behavior [45,46,50] of the intensive and broad 2 eV band in all the manganites investigated point to its inter-site d–d CT character, or strictly speaking, to the low energy HS e_g–e_g CT transition. Such a conclusion is strongly supported by proper quantitative estimates [45,46,56].

The intensity and energy position of four narrow bands forming the fine structure of 2 eV feature agree surprizingly well with the theoretical predictions (see Sec. 2 and Ref. 34) for the forbidden $t_{1g}(\pi) \to e_g$ and weakly-allowed $t_{2u}(\pi) \to e_g$ one-center p–d CT transitions splitted by a near tetragonal crystal field. The relative sharpness of all the weak p–d CT bands agrees with a localized character of nonbonding oxygen O2$p\pi$ orbitals. The most intensive and broad high-energy band modeled by four Lorentzians peaked at 3.0, 3.9, 4.65, and 5.3 eV [55] can be unambiguously assigned to the one-center dipole-allowed p–d CT transitions: $t_{1u}(\pi)$–$e_g(\pi-\sigma)$, $t_{2u}(\pi)$–$t_{2g}(\pi-\pi)$, $t_{1u}(\sigma)$–$e_g(\sigma-\sigma)$ transitions, respectively, with a hardly resolved low-symmetry splitting for the most intensive and broad bands.

It is worth noting that the assignment of p–d and d–d CT transition is of great importance for ZSA (Zaanen, Sawatzky, and Allen [57]) classification scheme usually applied for strongly correlated 3d compounds. As concerns the ZSA classification for perovskite manganites the situation seems to be far from being resolved. The parent compound $LaMnO_3$ is sorted either into the charge transfer insulator [43,48] or the Mott–Hubbard insulator [45–47,50,54].

Interestingly, that in the study by Arima *et al*. [48] $LaMnO_3$ is addressed to be located in the vicinity of the borderline where the optical gap changes from the Mott gap to the charge transfer gap that implies its dual nature. Our theoretical analysis and experimental data support this conjecture and evidence a dual nature of the dielectric gap in perovskite manganites $RMnO_3$, being formed by a superposition of *p–d* CT transitions and inter-site *d–d* CT transitions. In fact, the parent perovskite manganites $RMnO_3$ should rather be sorted neither into the CT insulator nor the Mott–Hubbard insulator in the ZSA scheme.

4.2. Hexagonal manganites $RMnO_3$

In the hexagonal phase of $RMnO_3$, each Mn ion occupies an unusual position formed by three in-plane and two apical oxygen ions fresulting in a MnO_5 trigonal bipyramid [58]. The crystal structure can be roughly represented by corner-shared MnO_5 bipyramids, which form a Mn^{3+} triangular lattice along the *ab* plane. However, there is an additional distortion because three MnO_5 bipyramids are tilted towards the oxygen ions at the center.

All the molecular orbitals in MnO_5 bipyramids with D_{3h} symmetry can be classified on a_1, a_2', a_2'', e', and e'' representations of the D_{3h} point group. Five 3*d* orbitals of the Mn^{3+} ion form a basis of $a_1(\propto d_{z2})$, $e'(\propto d_{xz,yz})$, and $e''(\propto d_{xy,x^2-y^2})$ representations. Nine in-plane oxygen O2*p* atomic orbitals form both σ-type $a_1(\propto d_{z2})$, $e''(\propto d_{xy,x^2-y^2})$ and π-type a_2', $a_2''(\propto p_z)$, $e'(\propto d_{xz,yz})$, $e''(\propto d_{xy,x^2-y^2})$ molecular orbitals. Six apical oxygen O2*p* atomic orbitals form σ-type $a_1(\propto d_{z2})$, $a_2''(\propto p_z)$ and π-type $e'(\propto p_{x,y})$, $e''(\propto d_{xz,xz})$ molecular orbitals. It is worth noting that all these orbitals do not have odd or even parity, that strongly affects the selection rules for electromagnetic transitions. All the orbitals with the same symmetry hybridize with each other thus forming bonding and antibonding molecular orbitals. The energy of the antibonding *d*-type singlet $a_1(d_{z2})$ in hexagonal $RMnO_3$ turns out to be always the highest in energy because namely this orbital is expected to be unoccupied for the high-spin state of Mn^{3+} ion. The energy of antibonding *d*-type doublet $e''(\propto d_{xy,x^2-y^2})$ is higher than that of the $e'(d_{xz,yz})$ doublet [59]. The selection rules for the dipole-allowed transitions to $a_1(d_{z2})$ state imply the initial $a_2''(\propto p_z)$ orbital for $\mathbf{E} \parallel \mathbf{c}$ polarization and $e''(\propto p_{x,y})$ orbital for $\mathbf{E} \perp \mathbf{c}$ polarization, respectively. In other words, one should expect two dipole-allowed transitions for $\mathbf{E} \parallel \mathbf{c}$ polarization and four dipole-allowed transitions for $\mathbf{E} \perp \mathbf{c}$ polarization.

The spectra of the real ε^{xx} and the imaginary ε^{zz} components of the dielectric tensor for yttrium manganite $YMnO_3$ are shown in Fig. 5 [60]. They are characterized by strong optical anisotropy in the entire spectral region under study. Strong suppression of the spectral weight for the narrow absorption band at 1.6 eV in ε_2^{zz} as compared with ε_2^{xx} and also the emergence of a wide absorption band at 3.5 eV in ε_2^{zz} should be specially noted Below 1.2–1.3 eV, the absorption drops to zero, which is in agreement with the direct transmission measurements of the absorption spectrum. An abnormally intense and narrow absorption band of ε_2^{xx} in the region of 1.6 eV is the most pronounced feature of the spectra. This band exhibits asymmetry, and its decomposition demonstrates the occurrence of at least two components. The absorption in the region above 2.2–2.4 eV increases with increasing photon energy, and a broad absorption peak is observed in the energy region of 4.6–4.8 eV both in ε^{xx} and ε^{zz}.

Similar results were reported for $YMnO_3$ and other hexagonal manganites (see, e.g., $ScMnO_3$ and $ErMnO_3$ [60], $LuMnO_3$ [61], $GdMnO_3$, $TbMnO_3$, $DyMnO_3$, $HoMnO_3$ [59]).

There has been a debate on the origin of the sharp optical transition at 1.6 eV for $\mathbf{E} \perp \mathbf{c}$ polarization. One interpretation is that it comes from the charge transfer transition from the O2*p* to the Mn3*d* states [60,62,63]. The PES study [63] suggested that the highest occupied level has mainly O2*p* character, while the unoccupied level has

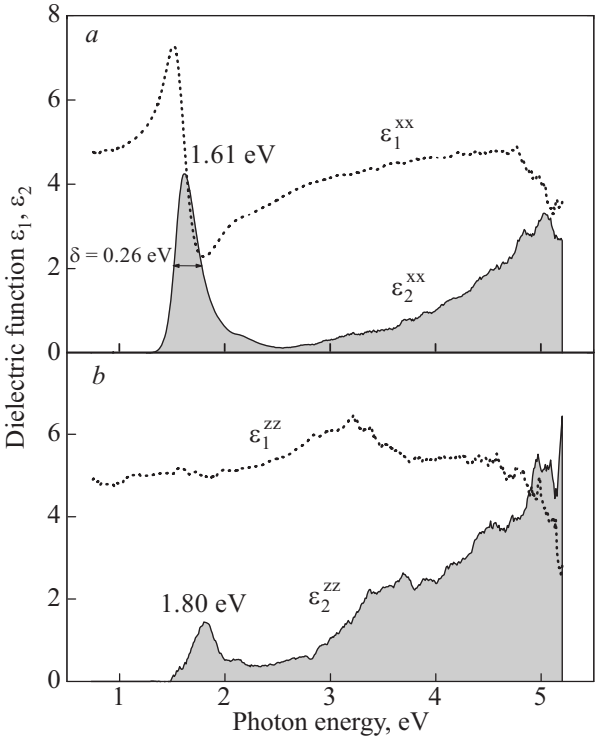

Fig. 5. Spectral dependences of the real and imaginary parts (dotted and solid lines, respectively) of the dielectric functions ε^{xx} (*a*) and ε^{zz} (*b*) for hexagonal $YMnO_3$.

Mn3*d* character. Other Mn3*d* states in the valence band are located at much lower energy, so that they cannot contribute to the optical transition at 1.6 eV. The other interpretation is that this peak comes from the on-site *d*–*d* transition $e''(d_{xy,x^2-y^2}) \to a_1(\propto d_{z2})$ between the Mn3*d* levels [61]. However, the *p*–*d* nature of the sharp 1.6 eV absorption peak seems to be more reasonable. It is supported both by its strong spectral weight typical for dipole-allowed *p*–*d* CT transitions and by different LDA+U calculations [59,62]. The band can be assigned to the interband optical CT transition from the high-energy predominantly in-plane oxygen O2*p* π-type bonding state $e''(\propto p_{x,y})$ to the unoccupied $a_1(\propto d_{z2})$ Mn state. In such a case the strong and broad band above 5 eV can be assigned to the interband optical CT transition from the low-energy predominantly in-plane oxygen O2*p* σ-type bonding state $e''(\propto p_{x,y})$ to the same unoccupied $a_1(\propto d_{z2})$ Mn state.

The *p*–*d* nature of 1.6 eV band is supported by the temperature effects. Indeed, the 1.6 eV optical feature has a large blueshift of (≈ 0.15 eV) [61] associated with the antiferromagnetic short range spin correlations which can be ascribed to the effects of the strong *p*–*d* exchange interaction in the *p*–*d* CT state. The intersite *d*–*d* interpretation as a charge transfer transition between Mn neighbors is ruled out because the spin dependence of the charge transfer matrix elements would lead to a strong temperature dependence of its oscillator strength which is not observed.

The relatively weak optical feature at 1.8 eV in ε^{zz} spectra is obviously related with small distortions of MnO_5 bipyramid which make the $e''(d_{xy,x^2-y^2}) \to a_1(\propto d_{z2})$ transition dipole-allowed for $\mathbf{E} \| \mathbf{c}$ polarization. At the same time the distinctly visible band at 3.5 and 5 eV can be attributed to CT transitions $a_2''(\propto p_z) \to a_1(\propto d_{z2})$ from a_2'' orbitals formed by the in-plane and apical oxygen O2*p* states, respectively.

To date, the optical transitions that involve an empty *d*-electronic state have been attributed to either *d*–*d* or *p*–*d* transitions. Strictly speaking, such simple interpretations are not suitable for explaining the electronic structure of hexa-$RMnO_3$ materials. Due to the strong hybridized nature of the occupied states, we cannot attribute the optical transition in the hexagonal phase simply to strict *d*–*d* or *p*–*d* transitions. Instead, the optical transitions in hexa-$RMnO_3$ should be regarded as an interband charge transfer excitation from the oxygen states strongly hybridized with Mn 3*d* of the same symmetry to the Mn $a_1(\propto d_{z2})$ state.

4.3. Orthorhombic manganites RMn_2O_5

The mixed-valent compounds RMn_2O_5 crystallize in an orthorhombic structure, space group *Pbam* [64,65]. The $Mn^{4+}O_6$ octahedra share edges forming infinite chains along the *z* axis. Every two $Mn^{3+}O_5$ pyramids, doubly linked by oxygens, form a dimer unit Mn_2O_{10}. Four $Mn^{4+}O_6$ octahedra chains are linked by a dimer unit in the *xy* planes through two oxygen ions. The fourfold symmetry axis in the $Mn^{3+}O_5$ pyramids lies in the *xy* plane at an angle of about ± 24° to the *x* axis.

Figure 6 shows ε_1 (*a*) and ε_2 (*b*) room temperature spectra of $TbMn_2O_5$ for all three main light polarizations [25]. The most intensive optical absorption (see ε_2 spectra) is observed for light polarization along the *z* axis while the less intensive is observed for light polarization along the *x* axis. This strong optical anisotropy gives rise to a giant linear dichroism and birefringence. The lowest energy oscillator distinctly seen in the *x* polarization at the energy 1.7 eV defines the absorption edge near 1.4 eV. The visibly split oscillator at 2.26–2.38 eV is distinctly seen in all polarizations. The strongest band of $\varepsilon_{2z} \approx 10$ is located at 3.0 eV while for the two other polarizations it is several times weaker. A slightly weaker peak of $\varepsilon_{2y} \approx 8$ is found at 3.5 eV. A relatively weak maximum of $\varepsilon_{2x} \approx 3$ is revealed at 5.0 eV. The band at 3.4–3.5 eV is most intensive in the *y* polarization while that at 3.9–4.0 eV is equally intensive both in the *y* and *z* polarizations. However, it is hardly distinguishable for the *x* polarization. The band at 5.0–5.4 eV is distinctly visible only in the *x* polarization, whereas for the two other polarizations it forms a structureless broad feature.

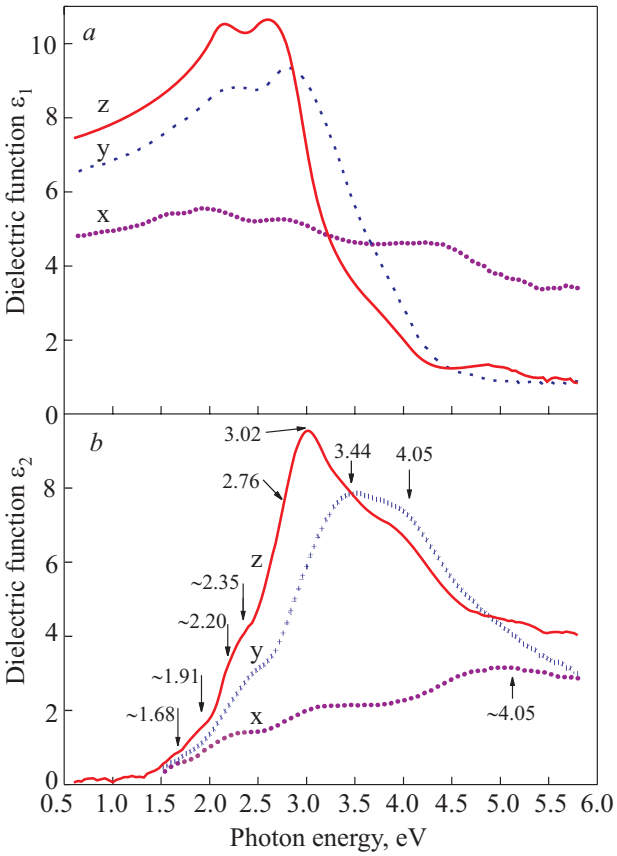

Fig. 6. Real ε_1 (*a*) and imaginary ε_2 (*b*) parts of the dielectric function in $TbMn_2O_5$. Arrows show positions of Lorentzian oscillators.

Intensive and broad bands observed in $TbMn_2O_5$ point to the *p–d* and *d–d* charge-transfer transitions as a main mechanism of optical response. A semiquantitative description of the *p–d* CT transitions in octahedral $Mn^{4+}O_6$ centers of RMn_2O_5 can be done with the use of a diagram of molecular orbitals and energies shown in Fig. 1 and the model theory presented in Sec. 2.

For the Mn^{3+} sublattice in $TbMn_2O_5$ we should consider strong parity-breaking effects and tetragonal distortions due to the fivefold pyramidal oxygen surrounding. Nevertheless, the scheme in Fig. 1 may be used for a qualitative analysis of *p–d* CT transitions in $Mn^{3+}O_5$ pyramids as well. The most important impact of the tetragonality consists in a large $d_{z2} - d_{x^2-y^2}$ splitting due to a strong decrease of the d_{z2} -level energy. The splitting can be estimated to be on the order of 1 eV. In addition, we deal with a strong rearrangement of electron states for nearby oxygen ions. In order to take into account this rearrangement careful band-like calculations are necessary. Nevertheless, simple symmetry considerations allow us to obtain very instructive information regarding the polarization properties of the *p–d* CT transitions in MnO_5 pyramidal clusters. Let us address the polarization properties of the main dipole-allowed one-center *p–d* CT transition $t_{1u}(\sigma) \to e_g$. The $t_{1ux,y}(\sigma) \to d_{x^2-y^2}$ transition is allowed only for the light polarized within the basal plane of MnO_5 pyramids, while the $t_{1uz}(\sigma) \to d_{z2}$ transition is allowed only for the light polarized along the local tetragonal axis of the MnO_5 pyramids. The former transition generates the absorption band with polarization properties in the crystal *xyz* coordinates as follows:

$$SW_x : SW_y : SW_z = \sin^2\theta : \cos^2\theta : 1 = 0.16 : 0.84 : 1.00, \tag{32}$$

where $SW_{x,y,z}$ is a spectral weight for the respective light polarization, $\theta \approx \pm 24^\circ$ is the angle between tetragonal axis of MnO_5 pyramids and the crystal *x* axis. The latter transition generates the absorption band with polarization properties as follows:

$$SW_x : SW_y : SW_z = \cos^2\theta : \sin^2\theta : 0 = 0.84 : 0.16 : 0. \tag{33}$$

The both Eqs. (32) and (33) can be used for a reliable assignment of the *p–d* CT transitions in the $Mn^{3+}O_5$ pyramids. We should note that the integral spectral weights for the one-center *p–d* CT transitions in octahedral MnO_6^{8-} and pyramidal MnO_5^{7-} centers are expected to be of comparable magnitudes.

In the mixed-valent manganites RMn_2O_5 there are four types of the two-center *d–d* CT transitions. The *d–d* CT transitions in Mn^{3+}–Mn^{3+} pairs, or dimer units Mn_2O_{10},

$$MnO_5^{7-} + MnO_5^{7-} \to MnO_5^{8-} + MnO_5^{6-} \tag{34}$$

imply the creation of electron MnO_5^{8-} and hole MnO_5^{6-} centers with electron configurations $t_{2g}^3 e_g^2$ and t_{2g}^3, formally related to Mn^{2+} and Mn^{4+}, respectively. The high-spin *d–d* CT transition can be represented as follows:

$$MnO_5^{7-}(t_{2g}^3 e_g^1; {}^5E_g) + MnO_5^{7-}(t_{2g}^3 e_g^1; {}^5E_g) \to$$

$$\to MnO_5^{8-}(t_{2g}^3 e_g^2; {}^6A_{1g}) + MnO_5^{6-}(t_{2g}^3; {}^4A_{2g}). \tag{35}$$

These transitions are only allowed if the polarization vector of the incident light **E** lies within the *xy* plane. The *d–d* CT transitions in Mn^{4+}–Mn^{4+} pairs imply the creation of electron MnO_6^{9-} and hole MnO_6^{7-} centers with electron configurations $t_{2g}^3 e_g^1$ and t_{2g}^2, formally related to Mn^{3+} and Mn^{5+}, respectively. The high-spin *d–d* CT transition can be represented as follows:

$$MnO_6^{8-}(t_{2g}^3; {}^4A_{2g}) + MnO_6^{8-}(t_{2g}^3; {}^4A_{2g}) \to$$

$$\to MnO_6^{9-}(t_{2g}^3 e_g^1; {}^5E_g) + MnO_6^{7-}(t_{2g}^2; {}^3T_{1g}). \tag{36}$$

These transitions are allowed only if **E** is parallel to the *z* axis. The two types of the *d–d* CT transitions in Mn^{4+}–Mn^{3+} pairs imply the creation of electron MnO_6^{9-} and hole MnO_5^{6-} centers with electron configurations $t_{2g}^3 e_g^1$ and t_{2g}^3, formally related to Mn^{3+}, and Mn^{4+} or electron MnO_5^{8-} and hole MnO_6^{7-} centers with electron configurations $t_{2g}^3 e_g^2$ and t_{2g}^2, formally related to Mn^{5+} and Mn^{2+}, respectively. Interestingly, the transfer energy in the former transition does not depend on the *dd* correlation parameter U_d, whereas the latter transition energy includes $2U_d$. At variance with the first two types of *d–d* CT transitions these are polarized in a more complicated way. As regards the quantitative estimates of the spectral weight for the *d–d* CT transitions in $TbMn_2O_5$ we expect several times weaker effects than those in $LaMnO_3$ due to respective scale of spin ordering temperatures and exchange integrals.

Turning to a comparison of theoretical predictions with our experimental data we should first point to an obvious relation

$$\varepsilon_{2x} < \varepsilon_{2y} < \varepsilon_{2z},$$

which holds almost over the whole spectral range under study. This unambiguously points to the one-center *p–d* CT transitions to the final $d_{x^2-y^2}$ state in MnO_5 pyramid as main contributors to the spectral weight. First, the spectral weights $SW_{x,y,z}$ obey nicely the ratio (32). The strongest band peaked near 3–4 eV may be attributed to the $t_{1ux,y}(\sigma) \to d_{x^2-y^2}$ transition. It should be noted that the line shape of the band actually depends on the rhombic distortions of $Mn^{3+}O_5$ pyramids lifting the $t_{1ux,y}(\sigma)$ dege-

neracy. Second, we do not see sizeable contributions of any two-center *d–d* CT transitions which are remarkable for their polarization properties. Third, the one-center *p–d* CT transitions in $Mn^{4+}O_6$ octahedra, being remarkable for the weak optical anisotropy, are likely displayed as a rather wide band peaked near 5 eV. It distinctly shows up in ε_{2x} where the $Mn^{3+}O_5$ pyramid contribution is strongly suppressed. Below main *p–d* CT bands we find several weak bands which may be related both to a number of weakly allowed *p–d* CT transitions and *d–d* CT transitions, which distinct assignment needs an additional experimental study.

5. Charge transfer spectroscopy of iron oxides

Experimental and theoretical investigations of the electronic structure of multiferroic $BiFeO_3$ and related iron oxides, in particular, the CT transitions, the band gap and in-gap states are of great importance for both a better scientific understanding as well as potential technological applications. Hereafter we report results of a comparative experimental spectroscopic study of the dielectric function of $BiFeO_3$ and several other related Fe^{3+} iron oxides with perovskite and more complicated crystal structures, and discuss the possible role of the *p–d* and *d–d* CT transitions.

5.1. Experimental data

5.1.1. Fe^{3+} *ions in octahedral positions*

Bismuth ferrite $BiFeO_3$. A large amount of literature has been published in recent years concerning the physical properties of bulk crystals and thin films of $BiFeO_3$, see, e.g., the most recent papers and references therein [18–20]. The experimental observations along with recent theoretical predictions of important electronic contributions to the multiferroic properties are a strong motivation for more detailed studies of its electronic structure. Very recent experimental studies [21,66,67] of $BiFeO_3$ are focused on the characterization of the band gap and near-band-gap states [19,20].

In the bulk form $BiFeO_3$ has a rhombohedrally distorted cubic perovskite cell and belongs to the $R3c$ space group [68–70]. Iron Fe^{3+} ions occupy noncentrosymmetric positions 6*c* with three short (1.952 Å) and three long (2.105 Å) Fe–O bonds. Fe^{3+} ions are shifted along the threefold axis by about 0.134 Å from the center of the oxygen octahedra. The antiferromagnetic ordering temperature $T_N = 643$ K and the ferroelectric temperature $T_C = 1143$ K [68].

There have been several measurements of the band gap of $BiFeO_3$ using UV-visible absorption spectroscopy and ellipsometry on polycrystalline $BiFeO_3$ films, epitaxial $BiFeO_3$ films grown by pulsed-laser deposition, nanowires, nanotubes, and bulk single crystals. Reported band gap values vary from 2.5 up to 2.8 eV [19–21,71,72]. Recent transmittance [21,71], absorption and cathodoluminescence spectra [66] revealed a low-energy near-band-gap optical feature near 2.5 eV. This was attributed to defect states due to oxygen vacancies though Basu *et al.* [21] could not discern whether the feature was related to a low-lying electronic structure or it had an excitonic character.

Our ellipsometric measurements were done from polished (001)-type surfaces with incident light polarizations along the [110], [110], and [100] directions. We observed optical anisotropy in the range of several percent but since the sample studied was most probably in a multidomain ferroelectric state we do not discuss it in this paper. We note that strong optical birefringence in $BiFeO_3$ was reported in Ref. 73. Figure 7,*a* shows the $\varepsilon', \varepsilon''$ spectra of $BiFeO_3$ [74]. Inset in Fig. 7,*a* shows the indices of absorption k and refraction n. Two groups of strong CT transitions are clearly seen around 3.0 and 4.0 eV. Note the enhanced structureless spectral weight in a wide range below the main CT bands with a remarkable smearing of the fundamental edge. The ε_2 value at 2.0 eV amounts almost to $\varepsilon_2 = 1.0$ which is an order of magnitude larger than in many other ferrites.

Orthoferrites. Orthoferrites $ErFeO_3$ and $Y_{0.95}Bi_{0.05}FeO_3$ belong to the distorted perovskite-type structure with the space group $Pbnm$. There are four Fe^{3+} ions in the unit cell in the centrosymmetric octahedral positions 4*b*. The Néel temperature lies in the range of 650 K. The $\varepsilon', \varepsilon''$ spectra of $ErFeO_3$ for three main polarizations shown in Fig. 8 are typical for the known spectra of orthoferrites $RFeO_3$ [31,32]. Two groups of intense bands are distinguished around 3.0 and 4.0 eV.

Spectra of orthoferrites differ from those of $BiFeO_3$ where the main bands are noticeably more intense, in par-

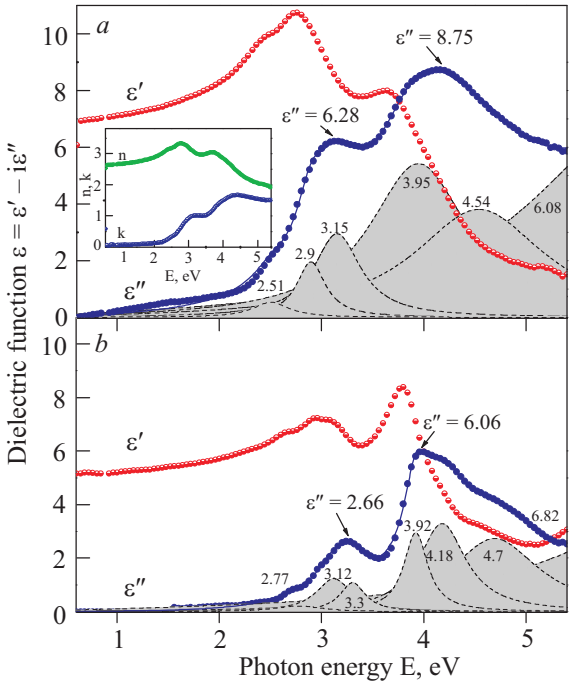

Fig. 7. (Color online) The dielectric functions and the contributing modes in $BiFeO_3$ (*a*). Inset shows indices of absorption and refraction. The dielectric function in orthoferrite $Y_{0.95}Bi_{0.05}FeO_3$ (*b*).

ticular the low-energy 3 eV band. This is well demonstrated in Fig. 7 where the optical spectra of the two perovskites $BiFeO_3$ and $Y_{0.95}Bi_{0.05}FeO_3$ are compared. At the same time we see in Fig. 7,*b* that 5% substitution of Y for Bi does not produce any noticeable changes in the spectra of orthoferrites.

Hematite α-Fe_2O_3. The hematite α-Fe_2O_3 is an iron oxide with the highest concentration of Fe^{3+} ions. The crystal structure is described by a rhombohedral space group $R\bar{3}c$. As in $BiFeO_3$, the Fe^{3+} ions occupy non-centrosymmetric positions 12*c* with three short (1.944 Å) and three long (2.113 Å) Fe–O bonds [75]. The Fe^{3+} ions are shifted along the threefold axis from the center of the oxygen octahedra. Each FeO_6 octahedron shares a face with another one in the layer above or below. High concentration and strong coupling between Fe^{3+} ions via oxygen ions leads to the high Néel transition temperature T_N = 948 K. Below this temperature α-Fe_2O_3 is piezomagnetic. Figure 9,*a* shows optical dielectric spectra of hematite for the incident light polarization in the basal plane. The dielectric spectra for two principal polarizations in gallium-substituted hematite α-$Fe_{2-x}Ga_xO_3$ are shown in Fig. 9,*b*,*c*. This material with x = 0.25 has the same trigonal crystal structure as hematite. General spectral features of these two materials are similar.

Iron borate Fe_3BO_6. This material crystallizes in an orthorhombic-type structure [76,77]. The space group is *Pnma* with four formula units per unit cell. The iron Fe^{3+} ions are located on two octahedral nonequivalent 4*c* and 8*d* sites coordinated by six oxygen O^{2-} ions. Both positions are strongly distorted in comparison to other ferrites. For 4*c* sublattice the Fe–O bond length varies from 1.865 to 2.226 Å, for the 8*d* sublattice from 1.905 to 2.131 Å. Iron ions form antiparallel spin arrangements within and between sublattices and Fe_3BO_6 is an antiferromagnet below T_N = = 508 K and a canted antiferromagnet below T_C = 430 K.

Optical spectra for three main polarizations are shown in Fig. 10,*a*,*b*,*c*. The strongest band at 3.06 eV is observed in the *b* polarization. In its general features the spectrum for this polarization looks similar to the hematite spectrum, see Fig. 9,*a*. The CT spectra for the *a* and *c* polarizations are less intense and resemble one another whereas the 3.06 eV band is suppressed. The observed strong trichroism is related to the low symmetry on both iron sites [78]. We note that the Fe_3BO_6 spectra radically differ from the known spectra of other iron borates. Optical transitions in Fe_3BO_6 are noticeably more intense and the band gap is red-shifted in comparison to other borates, $FeBO_3$ (T_N = = 348 K) and $GdFe_3(BO_4)_3$ (T_N = 37 K) [79,80]. These borates are highly transparent in the visible spectral range,

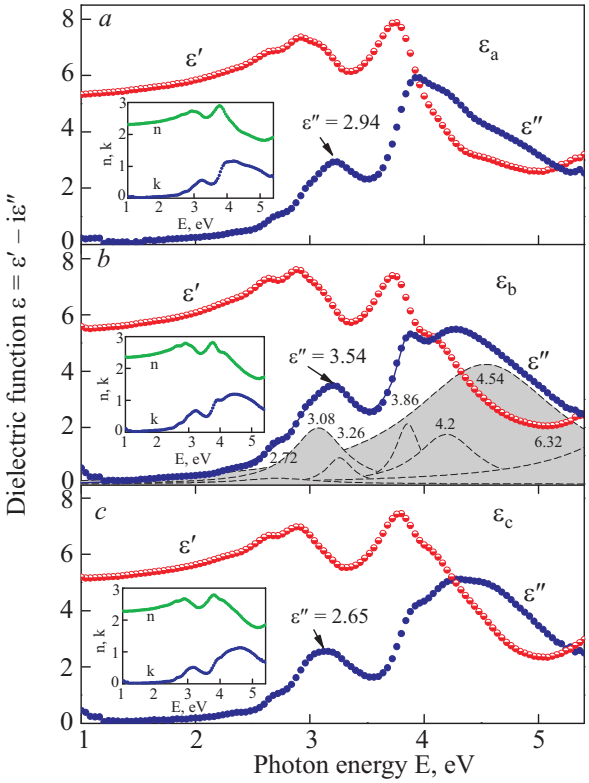

Fig. 8. (Color online) The dielectric function spectra in $ErFeO_3$ orthoferrite for three main polarizations. Insets show indices of absorption and refraction. Note, that the region below 1 eV is not shown because of strong interference effects, which occur due to the high transparency of the samples in this region.

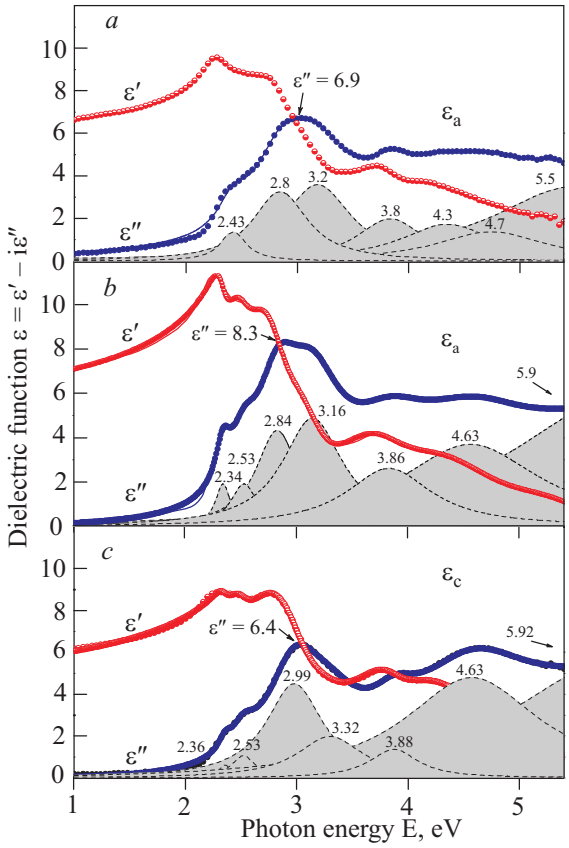

Fig. 9. (Color online) The dielectric function spectra of hematite α-Fe_2O_3 (*a*) and gallium-substituted hematite α-$Fe_{2-x}Ga_xO_3$ with x = 0.25 (*b*, *c*).

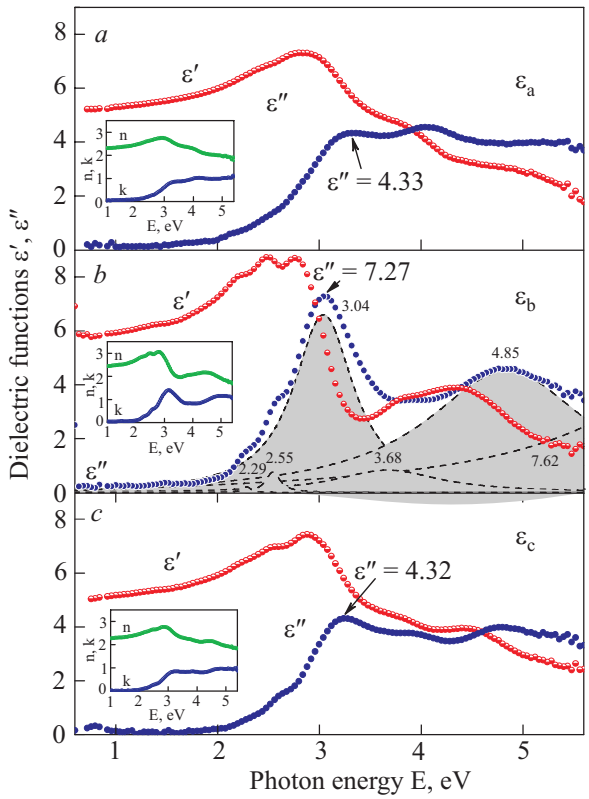

Fig. 10. (Color online) The dielectric function spectra of Fe_3BO_6 for the three main polarizations. Insets show indices of absorption and refraction.

the charge transfer bands are less intense and shifted to higher photon energy. The most plausible explanation of these differences can be related to the iron/oxide ratio which varies in these three compounds as 1/2, 1/3 and 1/4, respectively.

5.1.2. Fe^{3+} *ions in octahedral and tetrahedral positions*

All materials we discussed above contain magnetic Fe^{3+} ions only in octahedral positions. From a magnetic point of view they are antiferromagnets, or more strictly speaking, weak ferromagnets due to the canting of the antiferromagnetic sublattices derived from the Dzyaloshinsky–Moriya coupling and single-ion anisotropy. The materials we discuss below contain Fe^{3+} ions in octahedrally and tetrahedrally coordinated positions. Calcium ferrite is an antiferromagnet whereas all other materials are ferrimagnets due to the nonequivalency of the magnetic ions in the two types of positions. Our main goal is to elucidate the relative contribution to the optical response of the tetrahedral Fe^{3+} centers. To this end we address a series of ferrites with a rising fraction of tetrahedral Fe^{3+} centers.

Lithium ferrite $LiFe_5O_8$. Lithium ferrite $LiFe_5O_8$ has the cubic spinel structure, the space group $P4_332$ is noncentrosymmetric due to the one-to-three ordering of the Li- and Fe-ions on the octahedral sites [81]. The Fe^{3+} ions occupy the octahedral and tetrahedral crystallographic sites with a ratio of 4:1. Lithium ferrite has one of the highest ferromagnetic–paramagnetic transition temperature T_C = = 943 K which is remarkably close to that of hematite. $LiFe_5O_8$ is a material in which the linear magnetoelectric (ME) effect was reported [10]. A spontaneous nonreciprocal circular dichroism was observed in Ref. 11. Lithium ferrite is a promising candidate for multi-layered ferrimagnetic–ferroelectric composites exhibiting a large microwave magnetoelectric susceptibility [82]. Figure 11,*a* shows the dielectric functions measured on a polished (110) plate. It is worth noting that the optical spectra of $LiFe_5O_8$ resemble those of hematite. That points to a predominant contribution of the octahedral Fe^{3+} centers to optical transitions.

Hexaferrite $BaFe_{12}O_{19}$. Hexaferrites are a very large group of ferrimagnetic materials with a hexagonal structure where Fe^{3+} ions occupy slightly distorted octahedral and tetrahedral positions. In barium hexaferrite $BaFe_{12}O_{19}$ (magnetoplumbite) the Fe^{3+} ions occupy 9 octahedral, 2 tetrahedral, and one fivefold position. The experimental optical spectra for the (0001) face of a single crystal and a thin (~1 μ) polycrystalline film are shown in Fig. 11,*b*.

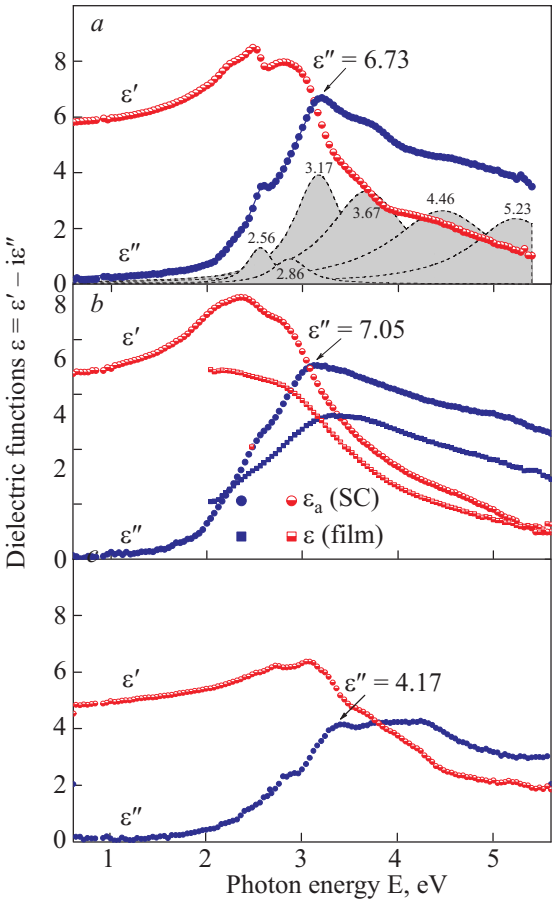

Fig. 11. (Color online) The dielectric function spectra of several ferrites with octahedral and tetrahedral Fe^{3+} centers: lithium ferrite $LiFe_5O_8$ (*a*), hexaferrite $BaFe_{12}O_{19}$ (*b*), rare earth garnet $Sm_3Fe_5O_{12}$ (*c*). For $BaFe_{12}O_{19}$ spectra of ε′ were measured for a single crystal (SC) and a polycrystalline thin film (film).

Predominance of the octahedral positions makes the optical response in $BaFe_{12}O_{19}$ similar to that of $LiFe_5O_8$ and hematite.

Rare earth garnet $Sm_3Fe_5O_{12}$. Garnets possess the cubic structure *Ia3d* with 8 formula units in the unit cell. Fe^{3+} ions occupy slightly distorted octahedral 24*c* positions and tetrahedral 16*a* positions with a ratio of 3:2. Iron garnets are ferrimagnetic and the ordering temperature of iron sublattices are in the range of about 550 K. Experimental spectra of optical dielectric functions in $Sm_3Fe_5O_{12}$ are shown in Fig. 11,*c*. In general features they are similar, but not exactly the same, as those reported in Refs. 83, 84.

Calcium ferrite $Ca_2Fe_2O_5$. This ferrite crystallizes in the orthorhombic space group of the brownmillerite type *Pnma* [85]. The Fe^{3+} ions occupy the octahedral 4*a* and tetrahedral 4*c* crystallographic sites with a ratio of 1:1. The Fe–O distances in the octahedral positions are 1.963 Å ($4O^{2-}$) and 1.977 Å ($2O^{2-}$). For the tetrahedral sites these are 1.884 Å ($2O^{2-}$), 1.858 Å, and 1.859 Å. These data show that both positions are only slightly distorted, e.g., compare them with data given above for the iron borate. Calcium ferrite is an antiferromagnet with $T_N = 725$ K, see Refs. 68, 86 and references therein. The dielectric spectra in the calcium ferrite for three principal polarizations are shown in Fig. 12. At first sight, in $Ca_2Fe_2O_5$ with the same content of octa- and tetrahedral centers, one should expect a competition of comparable contributions of the CT transitions related with octa- and tetrahedral Fe^{3+} centers. However, we see that the spectra differ from all the spectra discussed above, in particular, from those of lithium ferrite and magnetoplumbite where iron ions are also in octahedral and tetrahedral positions. Unexpectedly we observe a very strong CT-like band peaked near 0.5 eV that was not reported earlier. The 3.0 eV band, a visiting card of octahedral Fe^{3+} centers, is strongly suppressed due to a puzzling spectral weight transfer to the mid-infrared range. The spectra of $Ca_2Fe_2O_5$ for *a* and *c* polarizations are less intense, resemble one another but are not identical. Pronounced optical anisotropy could be related to the crystallographic features of $Ca_2Fe_2O_5$ having a pseudo-quadratic layered structure, see Figs. 2 and 3 in Ref. 85. It is worth noting that magnetic structure of $Ca_2Fe_2O_5$ is still a matter of debate [86–88].

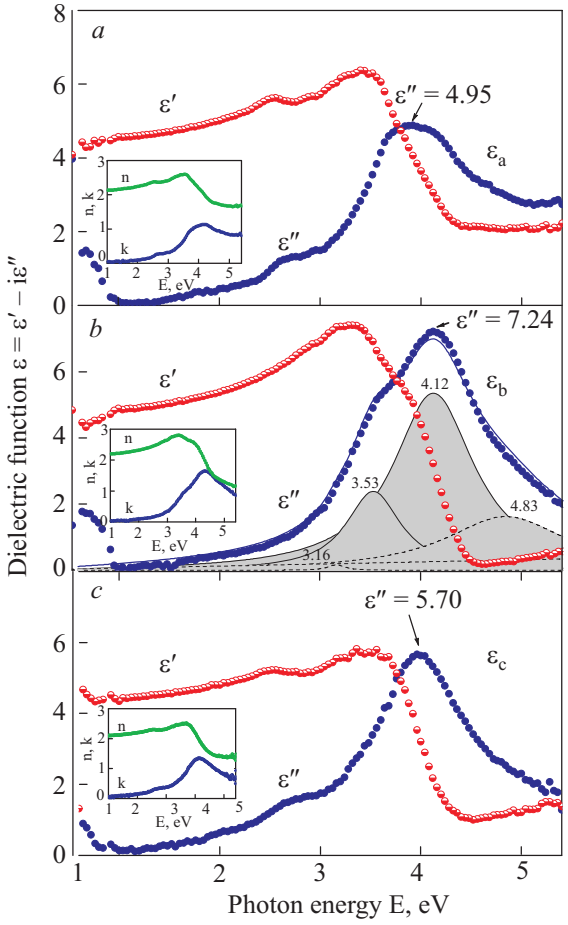

Fig. 12. (Color online) The dielectric function spectra in calcium ferrite $Ca_2Fe_2O_5$ for three main polarizations. Insets show indices of absorption and refraction.

5.2. Discussion

To begin our discussion of the CT transitions in ferrites we refer to the spectroscopic data for garnets $Y_3Fe_xGa_{5-x}O_{12}$ (x = 5, 3.9, 0.29, 0.09) [83]. They demonstrate that the optical response in the spectral range up to 30 000 cm^{-1} (~ 3.7 eV) is governed by the one-center transitions for both octahedral and tetrahedral Fe^{3+} centers. It means that the onset energy for different *d–d* CT transitions in ferrites is expected to be > 3.7 eV in agreement with our model estimates discussed in Sec. 3.

To uncover the role played by the octahedral Fe^{3+} centers we turn to the optical response of the orthoferrites $RFeO_3$. These compounds contain the only type of centrosymmetric, slightly (~1%) distorted, FeO_6 octahedra. Despite the long story of optical and magneto-optical studies (see, e.g. Refs. 32, 40) the microscopic origin of the main spectral features in orthoferrites remains questionable and the transition assignments made earlier in Ref. 32 need a comprehensive revisit. The spectra of $ErFeO_3$ for three main polarizations shown in Fig. 8 are typical for orthoferrites $RFeO_3$ [31,32,40]. The low-energy intense band around 3 eV may be assigned to a strong dipole allowed on-center $t_{2u}(\pi) \to t_{2g}$ CT transition as was proposed in Ref. 32. This is a characteristic feature of the octahedral Fe^{3+} centers in oxides, with the calcium ferrite being a puzzling exception. However, such an assignment also implies the existence of a weak band due to a low-energy dipole-forbidden on-center $t_{1g}(\pi) \to t_{2g}$ CT transition, red-shifted by about 0.8 eV as expected from estimates [35]. Indeed, a band around 2.5 eV is found in the optical and magneto-optical spectra of different orthoferrites [32]. This band is clearly visible in hematite α-Fe_2O_3 near 2.4 eV (see Fig. 9) where the $t_{1g}(\pi) \to t_{2g}$ transition becomes

allowed due to a breaking of the centrosymmetry for Fe^{3+} centers.

The nearest high-energy neighborhood of the 3 eV band is expected to be composed of $t_{1u}(\pi) \to t_{2g}$ CT transitions with a comparable intensity and estimated energy about 4 eV. All the dipole-allowed one-center *p–d* CT transitions to the e_g state are blue-shifted by $10\,Dq(3d^5)$ as compared to their $\gamma \to t_{2g}$ counterparts with the onset energy of the order of 4 eV. Interestingly, for the dipole-allowed $\gamma_u \to t_{2g}$ transitions the maximum intensity is expected for the low-energy $t_{2u}(\pi) \to t_{2g}$ transition while for $\gamma_u \to e_g$ transitions the maximum intensity is expected for the high-energy (~ 6–7 eV) $t_{1u}(\sigma) \to e_g$ transition. The analysis of the experimental spectra for orthoferrites demonstrates the failure of the one-center *p–d* CT transitions to explain the broad intensive band centered near 4.5 eV together with a narrow low-energy satellite peaked near 3.9 eV. Both features are typical for orthoferrites [32,40] and may be assigned to a $e_g \to t_{2g}$ low-energy two-center CT transition $^6A_{1g}{}^6A_{1g} \to {}^5E_g{}^5T_{2g}$ to an unconventional final state with an orbital degeneracy on both sites. These Jahn–Teller excited states are responsible for the complex lineshape of the $e_g \to t_{2g}$ CT band which is composed of a narrow exciton-like feature and a broad intense band separated by ~0.5 eV, which is believed to be a measure of the Jahn–Teller splitting in the excited state. Thus we see that all the spectral features observed in the optical spectra of orthoferrites for energies below 5 eV can be directly assigned to the low-energy *p–d* and *d–d* CT transitions.

It is worth noting that the dielectric function in orthoferrites is nearly isotropic due to very weak (~ 1%) rhombic distortions of FeO_6 octahedra and nearly equivalent different Fe–O–Fe bonds. Nevertheless a fine structure of the main CT bands is clearly revealed in magneto-optical spectra of orthoferrites, which was assigned to the dipole-forbidden *d–d* crystal field transitions [32,40]. In our opinion, their relation to the low-symmetry distortions in the *p–d* CT band seems to be more reasonable.

The effect of a strong change in bulk crystalline symmetry and local trigonal noncentrosymmetric distortions of FeO_6 octahedra is well illustrated by the optical response of hematite α-Fe_2O_3. First of all there is a noticeable rise of intensity and a splitting for dipole-forbidden $t_{1g}(\pi) \to t_{2g}$ transition at 2.4 eV, which is clearly visible in the spectra of the gallium-substituted sample (Fig. 9,*b*,*c*). Second, one should note a clear splitting on the order of 0.3–0.4 eV of the 3 eV band due to a sizeable trigonal distortion of the FeO_6 octahedra. In both cases the band splitting effect reflects the singlet-doublet splitting of the initial orbital triplets, $t_{1g}(\pi)$ and $t_{2u}(\pi)$, respectively, due to the low-symmetry trigonal crystal field. Interestingly, the integral intensity of the $t_{2u}(\pi) \to t_{2g}$ band at 3 eV is visibly enhanced in hematite as compared to similar bands in orthoferrites that may result from the more covalent Fe–O bonding in hematite. Such an explanation agrees with the increase in the Fe–O–Fe exchange coupling and higher values of T_N.

The optical spectrum of rhombohedral $BiFeO_3$ differs significantly from that of orthorhombic orthoferrites $RFeO_3$ in several points. It mostly resembles that of rhombohedral hematite α-Fe_2O_3 with an additional broad intense band centered near 4 eV, which may be assigned to CT transitions in the Bi–O bonds. The close relation with the hematite spectra is a direct result of the close similarity in the rhombohedral and non-centrosymmetric distortions of the FeO_6 octahedra in both compounds. It is worth noting that the Lorentzian fitting distinctly points to a small shoulder centered at 2.5 eV. This feature can be unambiguously attributed to the dipole-forbidden $t_{1g}(\pi) \to t_{2g}$ CT transition, similar to other ferrites with FeO_6 centers. Such a feature was observed in earlier studies [21,72], however without any explanation. Most recent absorption and cathodoluminescence spectra [66] reveal a fine three-peak structure of the 2.5 eV band in full accordance with low-symmetry (monoclinic) distortions of the epitaxial thin films. The authors attributed these observations to defect states due to oxygen vacancies, however, we relate their intrinsic nature to a low-lying $t_{1g}(\pi) \to t_{2g}$ CT transition typical for all other ferrites with octahedral FeO_6 centers.

The LSDA, LSDA+U [89], and sX [90] calculations show that the valence band of $BiFeO_3$ is formed predominantly by 2*p* oxygen states hybridized with the Fe 3*d* and Bi 6*p* states. The lowest conduction band is formed by the Fe 3*d* states with a DOS peak at 3.0 eV followed by the Bi 6*p* states with a DOS distributed from 3 to 6 eV. Most recent calculations give an indirect band gap E_g = 2.8 eV [90]. In contrast to direct-band semiconductors, a strict definition of the band-gap value E_g in transition metal compounds from experimental data is not straightforward. It is complicated by the absence of a sharp absorption edge and therefore depends on the procedure adopted. The experimental estimate based on optical absorption measurements in $BiFeO_3$ thin films gives a band-gap E_g = 2.5 eV [71]. More recent estimates give a direct band gap E_g = 2.7 eV [21,66,67] or E_g = 2.8 eV [72]. However, this kind of estimate is strongly dependent on sample morphology and quality. The low-energy optical response in bismuth ferrite $BiFeO_3$ reveals puzzling features, pointing to a CT instability in that oxide.

Despite the orthorhombic crystal symmetry of the iron borate Fe_3BO_6 its optical response resembles in general features that of trigonal hematite, but not that of orthoferrites. One should note a strong anisotropy especially pronounced for the low-energy intense $t_{2u}(\pi) \to t_{2g}$ band which looks like a solitary band at 3 eV in the b polarization (Fig. 10,*c*) and transforms into a plateau for the a and c polarizations, seemingly composed of two bands peaked at 3.2 and 4.2 eV. Such a strong anisotropy indirectly supports the *p–d* CT nature of the optical response. Indeed, unusually strong, up to ~ 20%, distortions of FeO_6 octahe-

dra in Fe_3BO_6 [76,77] imply a large low-symmetry splitting of both the initial $t_{2u}(\pi)$ and final t_{2g} states. The resultant effect may be strong enough to explain a splitting of the order of 1 eV. Iron borate spectra provide again a clear evidence of the 2.5 eV band assigned to dipole-forbidden *p–d* CT transitions $t_{1g}(\pi) \to t_{2g}$. Indeed, the well pronounced low-energy spectral features are clearly seen at 2.26 and 2.56 eV in *b* polarization. Most probably the low-symmetry effects are the main source responsible for the crucial difference in the optical response between Fe_3BO_6 and two other iron borates $FeBO_3$ (T_N = 348 K) and $GdFe_3(BO_3)_4$ (T_N = 37 K) [79,80]. These two borates are highly transparent in the visible spectral range and the CT bands are less intense and shifted to higher photon energy. Interestingly that, at variance with most of ferrites where the Fe–O–Fe bonds form a 3D network, the main motives of the crystal structure in $GdFe_3(BO_3)_4$ are spiral chains of FeO_6 octahedra running along the *c* axis and linked together by their edges. The antiferromagnetic ordering of the Fe subsystem occurs at about 37 K. In such a system one might observe the *d–d* CT transitions for the polarization $\mathbf{E} \| \mathbf{c}$ axis. Indeed, the absorption spectrum of $GdFe_3(BO_3)_4$ reveals an intensive band peaked near 4.8 eV observed for $\mathbf{E} \| \mathbf{c}$ axis [80], which may be attributed to the $e_g - t_{2g}$ CT transition in pairs of Fe^{3+} ions running along the *c* axis.

The optical response of ferrites containing both octahedral FeO_6 and tetrahedral FeO_4 centers is more complicated for a comprehensive analysis. First of all, we should point to a sizeable (~0.5 eV) blue shift of the onset energy for the *p–d* CT transitions in tetrahedral FeO_4 centers as compared to the octahedral FeO_6 centers [91,92]. This makes the low-energy optical response in such ferrites to be similar to that of ferrites with only octahedral FeO_6 centers.

Optical spectra of $LiFe_5O_8$ resemble those of hematite up to a quantitative agreement. Low-energy spectral features at 2.4 and 2.56 eV coincide with those observed in the spectral dependencies of its circular dichroism [11] and linear Kerr effect [93]. They were assigned to the *d–d* transitions in the Fe^{3+} ions in the octahedral and tetrahedral positions, respectively. However, their assignment to a split dipole-forbidden $t_{1g} - t_{2g}$ CT transition seems to be more reasonable, especially because such 2.5 eV band is typical for other octa/tetra ferrites (see Figs. 11, 12).

The optical response of calcium ferrite $Ca_2Fe_2O_5$ reveals a striking difference from the spectra of all other materials discussed above. The most noticeable feature is a strong suppression of the «octahedral» 3 eV band with a puzzling red shift of the respective spectral weight, which forms an extensive low-energy tail of the 3 eV band and anomalously strong mid-infrared band peaked below 1 eV. Both anomalies are believed to indicate a well developed CT instability of calcium ferrite due to self-trapping of the *p–d* CT excitons in octahedral Fe^{3+} centers, similar to that of bismuth ferrite [74]. The strong red shift of their spectral

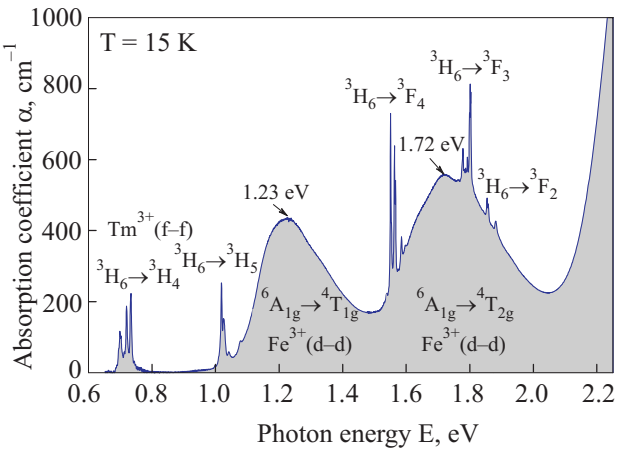

Fig. 13. Spectral dependence of the absorption coefficient for orthoferrite $TmFeO_3$.

weight for the respective *p–d* CT excitons makes manifestation of tetrahedral FeO_4 centers more pronounced. The significant optical anisotropy observed in $Ca_2Fe_2O_5$ can be attributed to a manifestation of the inter-layer octa-tetra *d–d* CT transitions with the $\mathbf{E} \| \mathbf{b}$ axis polarization. Indeed, calcium ferrite has a typical pseudoquadratic layered structure with alternating layers of highly symmetrical octahedral and tetrahedral Fe^{3+} centers having similar projections along the *a* and *c* axes, see Figs. 2 and 3 in Ref. 85. The peak energy of 4.1 eV for the respective band agrees with our estimates for *d–d* CT transitions.

In the discussion above we have focused on the more or less intensive CT bands, leaving out manifestations of the essentially weaker crystal field 3*d*–3*d* and 4*f*–4*f* transitions, part of which is superposed on the stronger CT bands. First of all it concerns a generic ${}^6A_{1g} \to {}^4A_{1g}$ transition which is usually superposed on the dipole forbidden $t_{1g}(\pi) - t_{2g}$ *p–d* CT transition. An instructive illustration of these weak features is presented in Fig. 13 where unpolarized absorption spectrum of the single crystalline $TmFeO_3$ is shown in the spectral range 0.6–2.2 eV for light propagated along the *c* axis [31]. As we see the absorption coefficient for the crystal field 3*d*–3*d* and 4*f*–4*f* transitions is about 2 orders of magnitude less than that typical for dipole-allowed CT transitions.

6. Conclusions

We have reviewed results of theoretical and experimental studies of CT transitions in the multiferroic manganites, ferrites and related complex oxides. Starting with a simple cluster model approach we addressed both the one-center *p–d* and two-center *d–d* CT transitions, their polarization properties, the role played by structural parameters, orbital mixing, and spin degree of freedom. The optical response was studied in a wide spectral range from 0.6 up to 5.8 eV by means of the spectroscopic ellipsometry. The oxides investigated have different crystal symmetry with more or

less distorted MnO_6 octahedra, two different types of MnO_5 centers, octahedral FeO_6 and tetrahedral FeO_4 centers. Manganites include orthorhombic RMn_2O_5, orthorhombic and hexagonal $RMnO_3$. One of the two groups of ferrites included $BiFeO_3$, $ErFeO_3$, $Y_{0.95}Bi_{0.05}FeO_3$, α-Fe_2O_3, $Fe_{2-x}Ga_xO_3$ and Fe_3BO_6 in which iron Fe^{3+} ions occupy only octahedral centrosymmetric or noncentrosymmetric positions with different magnitude of distortions from 1 to 20%. The second group included $LiFe_5O_8$, $BaFe_{12}O_{19}$, $Sm_3Fe_5O_{12}$, and $Ca_2Fe_2O_5$ in which Fe^{3+} ions occupy both octahedral and tetrahedral positions with a rising tetra/ortho ratio. At variance with several previous investigations we have performed a unified assignment of different dipole-allowed and dipole-forbidden CT transitions.

Experimental data and theoretical analysis evidence a dual nature of the dielectric gap in perovskite manganites, being formed by a superposition of forbidden $t_{1g}(\pi) \to e_g$ (1.3 and 1.9 eV) or weak dipole-allowed $t_{2u}(\pi) \to e_g$ (2.3 and 2.7 eV) *p–d* CT transitions and inter-site $d(e_g)$–$d(e_g)$ (2.0 eV in $LaMnO_3$ and 2.2 eV in other manganites) HS CT transitions, a remarkable observation, which to the best of our knowledge has not been previously reported. In fact, the parent perovskite manganites $RMnO_3$ should rather be sorted neither into the CT insulator nor the Mott–Hubbard insulator in the Zaanen, Sawatzky, Allen scheme. We found an overall agreement between experimental spectra and theoretical predictions based on the theory of one-center *p–d* CT transitions and inter-site *d–d* CT transitions. Spectral features at 3.0 and 3.8 eV are assigned to a weak dipole-allowed $t_{1u}(\pi) \to e_g$ *p–d* CT transition of the π–σ type with a clearly resolved low-symmetry splitting. Strong dipole-allowed *p–d* CT transitions $t_{1u}(\pi) \to t_{2g}$ and $t_{1u}(\sigma) \to e_g$ of the π–π and σ–σ type, respectively, are observed as the most intensive bands with an unresolved structure at 4.7 and 5.3 eV. Weak low-spin counterparts of the HS $d(e_g)$–$d(e_g)$ CT transition are seemingly superimposed on these strong *p–d* CT bands.

All the ferrites investigated are qualified to be CT insulators with the band gap determined by a dipole-forbidden $t_{1g} \to t_{2g}$ *p–d* CT transition near 2.5 eV, the spectral weight of which is strongly enhanced for the ferrites $BiFeO_3$ and α-Fe_2O_3 with noncentrosymmetric distortion of FeO_6 octahedra. In other words, the weak 2.5 eV band superimposed on the tail of the strong 3.0 eV band has a «non-defect» intrinsic nature and, along with its strong neighbor, can be regarded as a visiting card of the octahedral FeO_6 centers. It means we should revisit our view on the band gap structure in all iron oxides.

Intense bands near 3.0 and 4 eV are assigned to dipole allowed $t_{2u}(\pi) \to t_{2g}$ and $t_{1u}(\pi) \to t_{2g}$ *p–d* CT transitions in octahedral FeO_6 centers, respectively. The assignment of the low-energy two-center $e_g \to t_{2g}$ ${}^6A_{1g}{}^6A_{1g} \to {}^5E_g{}^5T_{2g}$ (*d–d*) CT transition to an unconventional Jahn–Teller-like final state, with an orbital degeneracy on both sites, is particularly manifested in the orthoferrite $ErFeO_3$ as an intense broad band peaked near 4.5 eV with a narrow low-energy satellite peaked at 3.9 eV. A noticeable enhancement of the optical response in $BiFeO_3$ at ~ 4 eV as compared to other related iron oxides is attributed to the CT transitions within the Bi–O bonds.

Along with an inspection of electron-hole excitations optical spectroscopy can provide a more direct information on the magnetoelectric coupling in multiferroics and related materials. Recently it has revealed a giant coupling of optical second-harmonic generation to the spontaneous polarization in compounds with magnetically driven ferroelectricity ($TbMn_2O_5$, $MnWO_4$) thus pointing to an electronic rather than ionic origin of the spontaneous polarization [94]. In $TbMn_2O_5$ the symmetry reduction by the ferroelectric order is detected with a sensitivity four orders of magnitude above the resolution limit of 10–100 pC/cm^2 [94]. Optical spectroscopy can provide an inaugural experimental statement on the controversial theoretical discussion on the nature of the multiferroic polarization [2,95].

Above we reviewed the CT spectra of different multiferroic manganites and ferrites though at present there are observations of the multiferroic behavior in several compounds with other 3*d* ions, such as $Ni_3V_2O_8$, $CuFe_{1-x}Al_xO_2$ [2]. Recent observations of multiferroic behavior concomitant the incommensurate spin spiral ordering in chain cuprates $LiCuVO_4$ [96] and $LiCu_2O_2$ [97] challenged the multiferroic community. At first sight, these cuprates seem to be prototypical examples of 1D spiral-magnetic ferroelectrics revealing the *relativistic* mechanism of «ferroelectricity caused by spin-currents» [98]. However, the both systems reveal a mysterious behavior with conflicting results obtained by different groups. Indeed, Yasui *et al*. [96] claim the $LiCuVO_4$ reveals clear deviations from the predictions of spin-current models. $LiCu_2O_2$ shows up a behavior which is obviously counterintuitive within the framework of spiral-magnetic ferroelectricity [97]. Moreover, recently it was shown [99,100] that the multiferroicity in $LiCuVO_4$ and $LiCu_2O_2$ may have nothing to do with *relativistic* effects and can be consistently explained, if the *nonrelativistic* exchange-induced electric polarization on the out-of-chain centers formed by a Cu^{2+} substitution for Li^+ ions in $LiCuVO_4$ or Cu^{2+} ions in $LiCu_2O_2$ is taken into account.

Optical response of multiferroic 1D cuprate $LiCu_2O_2$ has been measured by the ellipsometry method [101] and reflectivity [102]. Optical properties of $LiCu^{1+}Cu^{2+}O_2$ in the spectral range of 0.6–5.8 eV radically differ from those of all other known Cu^{1+}, Cu^{2+} and mixed-valent oxide cuprates. An extremely strong, sharp and highly anisotropic optical feature with $\varepsilon_2^{xx} = 26$ is observed at 3.27 eV which was assigned to an exciton-like inter-configurational 3*d*–4*p* transition in the O^{2-}–Cu^{1+}–O^{2-} dumbbells [101] rather than the *p–d* CT transition in $Cu^{2+}O_4$ plaquettes [102].

Concluding, we believe that the results of this review will provide deeper insight into the electronic structure of the multiferroic manganites and ferrites, other related compounds, and form a solid basis for further experimental and theoretical studies on the topic.

This work is supported in part by the Russian Foundation for Basic Research and State Contract No. 02.740.11.0384.

1. G.A. Smolenskii and I.E. Chupis, *Usp. Fiz. Nauk* **137**, 415 (1982); *Sov. Phys.-Uspekhi* **25**, 475 (1982).
2. M. Fiebig, *J. Phys*. **D38**, R123 (2005); M. Fiebig and N.A. Spaldin, *Eur. Phys. J*. **B71**, 293 (2009).
3. W. Eerenstein, N.D. Mathur, and J.F. Scott, *Nature* **442**, 759 (2006).
4. A.B. Harris, *Phys. Rev*. **B76**, 054447 (2007).
5. M. Fiebig, D. Fröhlich, S. Leute, K. Kohn, T. Lottermoser, V.V. Pavlov, and R.V. Pisarev, *Phys. Rev. Lett*. **84**, 5620 (2000).
6. T. Kimura, T. Goto, H. Shintani, K. Ishizaka, T. Arima, and Y. Tokura, *Nature (London)* **426**, 55 (2003).
7. N. Hur, S. Park, P.A. Sharma, J.S. Ahn, S. Guha, and S.-W. Cheong, *Nature (London)* **429**, 392 (2004).
8. K. Saito and K. Kohn, *J. Phys.: Condens. Matter* **7**, 2855 (1995).
9. H. Kimura, S. Kobayashi, S. Wakimoto, Y. Noda, and K. Kohn, *Ferroelectrics* **354**, 77 (2007).
10. G.T. Rado, *Phys. Rev. Lett*. **13**, 335 (1964).
11. V.N. Gridnev, B.B. Krichevtsov, V.V. Pavlov, and R.V. Pisarev, *JETP Lett*. **65**, 68 (1997).
12. B.B. Krichevtsov, V.V. Pavlov, and R.V. Pisarev, *JETP Lett*. **49**, 535 (1989).
13. T. Arima, D. Higashiyama, Y. Kaneko, J.P. He, T. Goto, S. Miyasaka, T. Kimura, K. Oikava, T. Kamiyama, R. Kumai, and Y. Tokura, *Phys. Rev*. **B70**, 064426 (2004).
14. K. Eguchi, Y. Tanabe, T. Ogawa, M. Tanaka, Y. Kawabe, and E. Hanamura, *J. Opt. Soc. Amer*. **B22**, 128 (2005).
15. A.M. Kalashnikova, R.V. Pisarev, L.N. Bezmaternykh, V.L. Temerov, A. Kirilyuk, and T. Rasing, *JETP Lett*. **81**, 452 (2005).
16. T. Kimura, G. Laves, and A.P. Ramires, *Phys. Rev. Lett*. **94**, 137201 (2005).
17. S. Ishiwata, Y. Taguchi, H. Murakava, Y. Onose, and Y. Tokura, *Science* **319**, 1643 (2008).
18. G. Catalan and J.F. Scott, *Adv. Mater*. **21**, 2463 (2009).
19. R. Palai, R.S. Katiyar, H. Schmid, P. Tissot, S.J. Clark, J. Robertson, S.A.T. Redfern, G. Catalan, and J.F. Scott, *Phys. Rev*. **B77**, 014110 (2008).
20. A.G. Gavriliuk, V.V. Struzhkin, I.S. Lyubutin, S.G. Ovchinnikov, M.Y. Hu, and P. Chow, *Phys. Rev*. **B77**, 155112 (2008).
21. S.R. Basu, L.W. Martin, Y.H. Chu, M. Gajek, R. Ramesh, R.C. Rai, X. Xu, and J.L. Musfeldt, *Appl. Phys. Lett*. **92**, 091905 (2008).
22. S. Picozzi, K. Yamauchi, B. Sanyal, I.A. Sergienko, and E. Dagotto, *Phys. Rev. Lett*. **99**, 227201 (2007).
23. A.S. Moskvin and S.-L. Drechsler, *Phys. Rev*. **B78**, 024102 (2008).
24. Y. Tanabe, T. Moriya, and S. Sugano, *Phys. Rev. Lett*. **15**, 1023 (1965).
25. A.S. Moskvin and R.V. Pisarev, *Phys. Rev*. **B77**, 060102(R) (2008).
26. Y. Tokura, *Rep. Prog. Phys*. **69**, 797 (2006).
27. R.M.A. Azzam and N.M. Bashara, *Ellipsompetry and Polarized Light*, North-Holland Publishing Company, Amsterdam (1977).
28. D.E. Aspnes, *J. Opt. Soc. Am*. **70**, 1275 (1980).
29. G.E. Jellison Jr., and J.S. Baba, *J. Opt. Soc. Am*. **A23**, 468 (2006).
30. A.M. Kalashnikova and R.V. Pisarev, *JETP Letters* **78**, 143 (2003).
31. P.A. Usachev, R.V. Pisarev, A.M. Balbashov, A.V. Kimel, A. Kirilyuk, and T. Rasing, *Phys. Solid State* **47**, 2292 (2005).
32. F.J. Kahn, P.S. Pershan, and J.P. Remeika, *Phys. Rev*. **186**, 891 (1969).
33. C.N.R. Rao and B. Raveau, *Transition Metal Oxides,* VCH (1995).
34. A.S. Moskvin, *Phys. Rev*. **B65**, 205113 (2002).
35. A.I. Liechtenshtein, A.S. Moskvin, and V.A. Gubanov, *Sov. Phys. Solid State* **24**, 2049 (1982).
36. D.A. Varshalovich, A.N. Moskalev, and V.K. Khersonskii, *Quantum Theory of Angular Momentum,* World Scientific, Singapore (1988).
37. E. Clementi and D.I. Raimondi, *J. Chem. Phys*. **38**, 2686 (1963); E. Clementi, D.I. Raimondi, and W.P. Reinhardt, *J. Chem. Phys*. **47**, 1300 (1967).
38. A.S. Moskvin and I.L. Avvakumov, *Physica* **B322/3–4**, 371 (2002).
39. B. Fromme, U. Brunokowski, and E. Kisker, *Phys. Rev*. **B58**, 9783 (1998).
40. J.H. Jung, K.H. Kim, D.J. Eom, T.W. Noh, E.J. Choi, J. Yu, Y.S. Kwon, and Y. Chung, *Phys. Rev*. **B55**, 15489 (1997); J.H. Jung, K.H. Kim, T.W. Noh, E.J. Choi, and J. Yu, *Phys. Rev*. **B57**, R11043 (1998).
41. Y. Okimoto, T. Katsufui, T. Ishikawa, A. Urushibara, T. Arima, and Y. Tokura, *Phys. Rev. Lett*. **75**, 109 (1995); Y. Okimoto, T. Katsufui, T. Ishikawa, T. Arima, and Y. Tokura, *Phys. Rev*. **B55**, 4206 (1997).
42. J.-S. Zhou and J.B. Goodenough, *Phys. Rev. Lett*. **96**, 247202 (2006).
43. K. Tobe, T. Kimura, Y. Okimoto, and Y. Tokura, *Phys. Rev*. **B64**, 184421 (2001).
44. N.N. Kovaleva, J.L. Gavartin, A.L. Shluger, et al., *JETP* **94**, 178 (2002).
45. N.N. Kovaleva, A.V. Boris, C. Bernhard, A. Kulakov, A. Pimenov, A.M. Balbashov, G. Khaliullin, and B. Keimer, *Phys. Rev. Lett*. **93**, 147204 (2004).
46. N.N. Kovaleva, A.M. Oleś, A.M. Balbashov, A. Maljuk, D.N. Argyriou, G. Khaliullin, and B. Keimer, *arXiv:0907.5098v1*.
47. M.W. Kim, S.J. Moon, J.H. Jung, Jaejun Yu, Sashin Parashar, P. Murugavel, J.H. Lee, and T.W. Noh, *Phys. Rev. Lett.* **96**, 247205 (2006).
48. T. Arima and Y. Tokura, *J. Phys. Soc. Jpn*. **64**, 2488 (1995).

49. K. Takenaka, K. Iida, Y. Sawaki, S. Sugai, Y. Moritomo, and A. Nakamura, *J. Phys. Soc. Jpn*. **68**, 1828 (1999).
50. M.A. Quijada, J.R. Simpson, L. Vasiliu-Doloc, J.W. Lynn, H.D. Drew, Y.M. Mukovskii, and S.G. Karabashev, *Phys. Rev*. **B64**, 224426 (2001).
51. N.N. Loshkareva, Yu.P. Sukhorukov, E.V. Mostovshchikova, L.V. Nomerovannaya, A.A. Makhnev, S.V. Naumov, E.A. Gan'shina, I.K. Rodin, A.S. Moskvin, and A.M. Balbashov, *JETP* **94**, 350 (2002).
52. M. Bastjan, S.G. Singer, G. Neuber, S. Eller, N. Aliouane, D.N. Argyriou, S.L. Cooper, and M. Rübhausen, *Phys. Rev*. **B77**, 193105 (2008).
53. J.F. Lawler, J.G. Lunney, and J.M.D. Coey, *J. Appl. Phys. Lett*. **65**, 3017 (1994).
54. M.W. Kim, P. Murugavel, Sashin Parashar, J.S. Lee, and T.W. Noh, *New J. Phys.* **6**, 156 (2004).
55. A.S. Moskvin, A.A. Makhnev, L.V. Nomerovannaya, N.N. Loshkareva, and A.M. Balbashov (*to be published*).
56. K.H. Ahn and A.J. Millis, *Phys. Rev*. **B61**, 13545 (2000).
57. J. Zaanen, G.A. Sawatzky, and J.W. Allen, *Phys. Rev. Lett*. **55**, 418 (1985).
58. T. Katsufuji, M. Masaki, A. Machida, M. Moritomo, K. Kato, E. Nishibori, M. Takata, M. Sakata, K. Ohoyama, K. Kitazawa, and H. Takagi, *Phys. Rev*. **B66**, 134434 (2002).
59. Woo Seok Choi, Dong Geun Kim, Sung Seok A. Seo, Soon Jae Moon, Daesu Lee, Jung Hyuk Lee, Ho Sik Lee, Deok-Yong Cho, Yun Sang Lee, Pattukkannu Murugavel, Jaejun Yu, and Tae W. Noh, *Phys. Rev*. **B77**, 045137 (2008).
60. A.M. Kalashnikova and R.V. Pisarev, *JETP Lett*. **78**, 143 (2003).
61. A.B. Souchkov, J.R. Simpson, M. Quijada, H. Ishibashi, N. Hur, J.S. Ahn, S.W. Cheong, A.J. Millis, and H.D. Drew, *Phys. Rev. Lett*. **91**, 027203 (2003).
62. J.E. Medvedeva, V.I. Anisimov, M.A. Korotin, O.N. Mryasov, and A.J. Freeman, *J. Phys.: Condens. Matter* **12**, 4947 (2000).
63. J.-S. Kang, S.W. Han, J.-G. Park, S.C. Wi, S.S. Lee, G. Kim, H.J. Song, H.J. Shin, W. Jo, and B.I. Min, *Phys. Rev*. **B71**, 092405 (2005).
64. J.A. Alonso, M.T. Casais, M.J. Martinez-Lope, and I. Rasines, *J. Solid State Chem*. **129**, 105 (1997).
65. A.F. Garcia-Flores, E. Granado, H. Martinho, R.R. Urbano, C. Rettori, E.I. Golovenchits, V.A. Sanina, S.B. Oseroff, S. Park, and S.-W. Cheong, *Phys. Rev*. **B73**, 104411 (2006).
66. A.J. Hauser, J. Zhang, L. Mier, R.A. Ricciardo, P.M. Woodward, T.L. Gustafson, L.J. Brillson, and F.Y. Yang, *Appl. Phys. Lett*. **92**, 222901 (2008).
67. J.F. Ihlefeld, N.J. Podraza, Z.K. Liu, R.C. Rai, X. Xu, T. Heeg, Y.B. Chen, J. Li, R.W. Collins, J.L. Musfeldt, X.Q. Pan, J. Schubert, R. Ramesh, and D.G. Schlom, *Appl. Phys. Lett*. **92**, 142908 (2008).
68. Landolt-Börnstein, *Numerical Data and Functional Relationships*, New Series, Group III, Condensed Matter, Springer-Verlag, Berlin (1984).
69. F. Kubel and H. Schmid, *Acta Cryst*. **B46**, 698 (1990).
70. A. Palewicz, R. Przenioslo, I. Sosnovska, and A.W. Hewat, *Acta Cryst*. **B63**, 537 (2007).
71. T. Kanai, S. Ohkoshi, and K. Hashimoto, *J. Phys. Chem. Solids* **64**, 391 (2003).
72. A. Kumar, R.C. Rai, N.J. Podraza, S. Denev, M. Ramirez, Y.H. Chu, L.W. Martin, J. Ihlefeld, T. Heeg, J. Schubert, D.G. Schlom, J. Orenstein, R. Ramesh, R.W. Collins, J.L. Musfeldt, and V. Gopalan, *Appl. Phys. Lett*. **92**, 121915 (2008).
73. J.P. Rivera and H. Schmid, *Ferroelectrics* **204**, 23 (1997).
74. R.V. Pisarev, A.S. Moskvin, A.M. Kalashnikova, and Th. Rasing, *Phys. Rev*. **B79**, 235128 (2009).
75. R.L. Blake, R.E. Hessevick, T. Zoltai, and L.W. Finger, *Amer. Mineralogist* **51**, 123 (1966).
76. J.G. White, A. Miller, and R.E. Nielsen, *Acta Crystallogr*. **19**, 1060 (1965).
77. R. Diehl and G. Brandt, *Acta Crystallogr*. **B31**, 1662 (1975).
78. B. Andlauer, R. Diehl, and M.S. Skolnik, *J. Appl. Phys*. **49**, 2200 (1978).
79. P.A. Markovin, A.M. Kalashnikova, R.V. Pisarev, and T. Rasing, *JETP Lett*. **86**, 712 (2007).
80. A.M. Kalashnikova, V.V. Pavlov, R.V. Pisarev, L.N. Bezmaternyukh, M. Bayer, and T. Rasing, *JETP Lett*. **80**, 293 (2005).
81. C. Wende and H. Langbein, *Crystallogr. Res. Technol*. **41**, 18 (2006).
82. M.I. Bichurin, V.M. Petrov, Yu.V. Kiliba, and G. Srinivasan, *Phys. Rev*. **B66**, 134404 (2002).
83. G.B. Scott, D.E. Lacklison, and J.L. Page, *Phys. Rev*. **B10**, 971 (1974).
84. S. Wittekoek, T.J.A. Popma, J.M. Robertson, and P.F. Bongers, *Phys. Rev*. **B12**, 2777 (1975).
85. E.F. Bertaut, P. Blum, and A. Sagniéres, *Acta Crystallogr*. **12**, 149 (1959).
86. P.A. Marchukov, R. Geick, C. Brotzeller, W. Treutman, E.G. Rudashevsky, and A.M. Balbashov, *Phys. Rev*. **B48**, 13538 (1993).
87. H.D. Zhou and J.B. Goodenough, *Solid State Sciences* **7**, 656 (2005).
88. C.B. Azzoni, M.C. Mozzatti, V. Massarotti, D. Capsoni, and M. Bini, *Solid State Sciences* **9**, 515 (2007).
89. J.B. Neaton, C. Ederer, U.V. Waghmare, N.A. Spaldin, and K.M. Rabe, *Phys. Rev*. **B71**, 014113 (2005).
90. S.J. Clark and J. Robertson, *Appl. Phys. Lett*. **90**, 132903 (2007).
91. A.S. Moskvin, A.V. Zenkov, E.I. Yuryeva, V.A. Gubanov, *Physica* **B168**, 186 (1991).
92. A.S. Moskvin, A.V. Zenkov, E.A. Ganshina, G.S. Krinchik, and M.M. Nishanova, *J. Phys. Chem. Solids* **54**, 101 (1993).
93. S. Viŝnovsky and R. Krishnan*, Appl. Phys*. **18**, 243 (1979).
94. Th. Lottermoser, D. Meier, R.V. Pisarev, and M. Fiebig, *Phys. Rev*. **B80**, 100101(R) (2009).
95. A.S. Moskvin and S.-L. Drechsler, *Phys. Rev*. **B78**, 024102 (2008); *Eur. Phys. J*. **B71**, 331 (2009).
96. Y. Naito, K. Sato, Y. Yasui, Yu. Kobayashi, Yo. Kobayashi, and M. Sato, *J. Phys. Soc. Jpn*. **76**, 023708 (2007).

97. S. Park, Y.J. Choi, C.L. Zhang, and S-.W. Cheong, *Phys. Rev. Lett*. **98**, 057601 (2007).
98. H. Katsura, N. Nagaosa, and A.V. Balatsky, *Phys. Rev. Lett*. **95**, 057205 (2005).
99. A.S. Moskvin and S.-L. Drechsler, *Europhys. Lett*. **81**, 57004 (2008).
100. A.S. Moskvin, Yu.D. Panov, and S.-L. Drechsler, *Phys. Rev*. **B79**, 104112 (2009).
101. R.V. Pisarev, A.S. Moskvin, A.M. Kalashnikova, A.A. Bush, and Th. Rasing, *Phys. Rev*. **B74**, 132509 (2006).
102. M. Papagno, D. Pacile, G. Caimi, H. Berger, L. Degiorgi, and M. Grioni, *Phys. Rev*. **B73**, 115120 (2006).